Solar Energy 282 (2024) 112936

Contents lists available at ScienceDirect

Solar Energy

journal homepage: www.elsevier.com/locate/solener

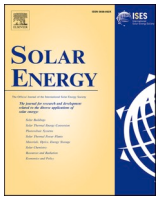

A comparison of secondary optic designs for linear Fresnel collectors with a single tubular absorber

André Santos [a,*], Diogo Canavarro [a], Camilo A. Arancibia-Bulnes [b], Pedro Horta [a], Manuel Collares-Pereira [a]

[a] University of Évora – Renewable Energies Chair, Polo Da Mitra Da Universidade de Évora, Edifício Ário Lobo de Azevedo, 7000-083 Nossa Senhora Da Tourega, Portugal

[b] Instituto de Energías Renovables, Universidad Nacional Autónoma de México, Privada Xochicalco, Col. Centro, Temixco 62580, Morelos, México

ARTICLE INFO

Keywords:
Linear Fresnel Collector
Secondary optics design
Optical analysis

ABSTRACT

This work presents a comparison of secondary optics for linear Fresnel collectors with a single absorber tube. The Compound Parabolic Concentrator (CPC) is indicated as the better secondary in different studies and under assessments including efficiency and flux uniformity, although it was never compared to the Compound Elliptical Concentrator (CEC) and to a recently proposed aplanatic design. Moreover, CPC geometries resulting from stochastic optimization needs to be confronted with theoretical edge-ray designs to evaluate the necessity of this optimization procedure. The ensuing ray-tracing results indicate that when the efficiency is the sole objective, CPC optimum geometry highly diverge from the edge-ray design, presenting a better efficiency but far lower performance in terms of flux uniformity and acceptance. In a two-objective problem involving efficiency and flux uniformity, optimum geometries for the CPC get closer to the edge-ray designs, particularly if the later considers the same gap size. Indeed, the gap size emerges as an important decision variable to play with the trade-off between the optical efficiency and flux uniformity. Comparison between CPC and CEC edge-ray designs shows that both optics in practice relate to a trade-off between optical efficiency and acceptance – the CPC presents a higher acceptance, the CEC has higher efficiency, whilst results of flux uniformity are practically the same. Regarding the aplanat design, it performs poorly in terms of acceptance angle compared to edge-ray designs, although outperforms them both in flux uniformity, and is outperformed by the CEC in terms of efficiency.

1. Introduction

The Linear Fresnel Collector (LFC) is a solar concentrator technology mainly used for thermal applications. It is composed of a primary field of reflectors slightly elevated from the ground whose purpose is to reflect (and concentrate) the incident sunlight on a fixed linear receiver located above the primaries [1,2]. Each heliostat has a single-axis tracking mechanism to follow the Sun's daily movement. The receiver has an absorber element to convert the reflected radiation to thermal energy, transferring it to a heat transfer fluid.

The receiver can also contain a secondary optic, whose shape is related to the absorber's [3]. Usually, a trapezoidal secondary is associated with a multi-tube absorber, while Compound Parabolic Concentrator (CPC) is associated with a single tube [4].

Previous studies have highlighted that secondary optics enhance the overall performance of LFCs [5–7]. In the case of high-temperature (>400 °C) applications such as solar thermal electricity [8,9], an evacuated tube [10] is the main absorber element due to its low thermal losses under such conditions [11,12]. Thus, this work considers secondary optic designs for LFCs with a single absorber tube, which could be encapsulated by a concentric (evacuated) glass cover. In this context, the literature comprises several propositions and a few comparison studies of secondary optics.

The Compound Parabolic Concentrator (CPC) is an optic proposed by Feuermann and Gordon [5] as a secondary for LFCs. This concentrator is an essential finding by Welford and Winston [13] in the development of the principles of Non-Imaging Optics (NIO) [14] – an ideal solution for a radiative source infinitely large at an infinite distance. Oomen and Jayaraman [15] took further developments for linear receivers [16,17] to present simple equations for the case of tubular absorbers. Later, Chaves [18] stated that this optic comprises involutes and macro focal parabolas – analytical plane curves derived from the edge-rays principle.

Grena and Tarquini [19] presented the Parabolic Wings Concentrator

* Corresponding author.
E-mail address: avas@uevora.pt (A. Santos).

https://doi.org/10.1016/j.solener.2024.112936
Received 5 July 2024; Received in revised form 19 August 2024; Accepted 11 September 2024
0038-092X/© 2024 International Solar Energy Society. Published by Elsevier Ltd. All rights are reserved, including those for text and data mining, AI training, and similar technologies.

Nomenclature

Latin characters

d	distance between two neighbor primary mirrors [m]
h_s	secondary optic height from the tube center [m]
k	aplanatic optic design parameter [-]
n^a_{rays}	number of final light rays striking the absorber [-]
r_a	absorber tube radius [m]
r_{gap}	gap size (or gap radius) [m]
r_{go}	radius of the glass outer cover [m]
q_i	flux density in the circumferential bin of index i [W/m^2]
q_{ray}	power carried by each light ray [W]
s	aplanatic optic design parameter [-]
w	primary mirror width [m]
A_{abs}	absorber tube surface area [m^2]
A_{net}	primary field mirror (net) area [m^2]
$\mathbf{F}_1$,$\mathbf{F}_2$	the edge-points of the primary field
H_R	absorber tube height [m]
L	concentrator length (in the longitudinal direction) [m]
NA	aplanatic optic design parameter [-]
N_{bins}	number of circumferential bins in which the absorber is divided [-]
Q_{abs}	absorbed flux in the receiver [W]
$\mathbf{T}_1$,$\mathbf{T}_2$	the edge-points of the absorber tube
W_a	aplanat primary optic aperture width [m]
W_p	primary field aperture width [m]
W_s	secondary optic aperture width [m]

Greek characters

α	absorptivity of the absorber tube [-]
β	LFC optic acceptance half-angle [degrees]
$\overline{\beta}$	annual average value of β [degrees]
δ_q	circumferential flux non-uniformity index [-]
$\overline{\delta}_q$	annual average value of δ [-]
η	LFC optical efficiency [-]
$\overline{\eta}$	annual average value of η [-]
θ_a	CPC optic acceptance half-angle [degrees]
θ_e	angular aperture defined by the intersection of edge-rays [degrees]
θ_{max}	maximum opening angle of a CPC secondary optic [degrees]
θ_L	longitudinal incidence angle [degrees]
θ_T	transversal incidence angle [degrees]
μ_q	average flux density at the absorber [W/m^2]
ρ_p	primary reflector reflectivity [-]
ρ_s	secondary reflector reflectivity [-]
σ_o	standard deviation of the overall Gaussian optical error [mrad]
σ_q	standard deviation of the circumferential flux distribution [W/m^2]
σ_s	standard deviation of a Gaussian slope error [mrad]
σ_{sp}	standard deviation of a Gaussian specular error [mrad]
σ_{sun}	standard deviation of a Gaussian sunshape [mrad]
σ_t	standard deviation of a Gaussian tracking error [mrad]
Δr_g	distance between glass outer cover and secondary optic: $r_{gap} - r_{go}$ [m]
Δ_{sun}	half-width of a pillbox sunshape [mrad]

Abbreviations

ASC	Adaptative Secondary Concentrator
AOC	Aplanatic Optic Concentrator
CAP	Concentration Acceptance Product
CEC	Compound Elliptical Concentrator
CPC	Compound Parabolic Concentrator
DPC	Double Parabolic Concentrator
DNI	Direct Normal Irradiation
EW	East-West
LFC	Linear Fresnel Collector
MCRT	Monte Carlo Ray-Tracing
NS	North-South
PWC	Parabolic Wings Concentrator
NA	Numerical Aperture of an aplanat optic
NIO	Non-Imaging Optics
RMS	Root mean square
SMS	Simultaneous Multiple Surfaces
SPC	Segmented Parabolic Concentrator
TMY	Typical Meteorological Year

(PWC) as a secondary optic to achieve a more homogeneous flux distribution on the absorber. The Simultaneous Multiple Surfaces (SMS) design by Canavarro et al. [20] encompasses the primary and secondary optics simultaneously without considering pre-defined shapes – it advances from a starting point to define both reflectors. Balaji et al. [21] have compared secondary optics presenting parabolic and involute profiles: efficiency and flux distribution results indicate that the former performs better.

Canavarro et al. [22] proposed an asymmetric secondary composed of involutes, V-grooves, and macro focal ellipses – the Compound Elliptical Concentrator (CEC) [18] – for LFCs with an asymmetric primary field. This design applies the edge-ray principle as referred above in the context of a finite radiative source at a finite distance.

Prasad et al. [7] have presented the Segmented Parabolic Concentrator (SPC) as the secondary optic. In this case, one symmetrical side of a parabola is split into two pieces, and the one farther away from the tube is then rotated. The authors compared this design to a Trapezoidal Secondary Concentrator (TSC) and a CPC to find the one presenting higher flux circumferential homogeneity and optical efficiency levels. At first, when primary mirrors have a fixed aim-line – the center of the absorber tube – the CPC optic presented better performance. However, with a variable aim-line (in the vertical direction), the SPC marginally outperforms the CPC, with the TSC being far worse than the previous two.

Zhu [23] proposed an adaptative design to define a secondary optic. This approach does not assume a pre-defined shape (involute, parabolic, trapezoidal, etc.) but adapts the surface contour step-by-step to yield the highest optical efficiency. Based on a starting point, this design defines the local slope that maximizes the fraction of the incoming flux from the primary field reflected towards the absorber tube. The next contour point is defined by advancing a tiny step in the direction given by the local slope, advancing up to the absorber symmetry axis.

Hack et al. [24] presented a comparison study of four secondary optics: the Adaptative Secondary Concentrator (ASC) proposed by Zhu [23], the CPC optic [15], the Trapezoidal Secondary Concentrator (TSC), and the Parabolic Wings Concentrator (PWC) proposed by Grena and Tarquini [19]. The results indicate that the ASC has the highest optical efficiency, marginally outperforming the CPC, and the others (PWC and TSC) are far worse than the previous two optics.

On the other hand, Hack's study [24] does not include metrics regarding flux circumferential uniformity or a fair range of the decision variables involved in the design of those secondaries, which might cloudy the optimum conditions.

To address these issues, Abbas et al. [25] presented a comparison of

three secondary technologies: the CPC optic [15], the Adaptative Secondary Concentrator (ASC) [23], and the Segmented Parabolic Concentrator (SPC) presented by Prasad et al. [7]. Results indicate that the best choice relies on the CPC and ASC optics, depending on constraints of minimum flux and flux homogeneity – the CPC achieves higher efficiencies when higher homogeneity is required; the ASC has better results when homogeneity and minimum flux are not strong constraints. Indeed, since the authors considered a fixed aim line for the primary mirrors tracking, these results agree with the findings of Prasad et al. [7], where the CPC outperforms the SPC. Furthermore, the authors highlighted that ASC and CPC optics have similar shapes.

Bellos et al. [26] did not propose a secondary optic design but used Bezier polynomials to parametrize an already-existent optic. Then, the manipulation of the control points of the Bezier curve is used to search for an optic with the highest optical efficiency at normal incidence.

Vouros et al. [27] presented a secondary optic design similar to Zhu's [23]. Instead of a point-by-point design, Vouros' approach is based on the sequential definition of the center point and the tilt of small flat segments to define the optic contour. Since these segments are tiny compared to absorber tube size, a reasonable assumption is to simplify them as points and the tilts as the local slopes – as in Zhu's method. Furthermore, Vouros' design determines the tilt of a segment by sampling reflected rays from the primary field and calculating the tilt which maximizes the number of rays that strike the receiver after a second reflection – a kind of ray-tracing approach; Zhu's method determines the local slope as the one which maximizes the fraction of the incident intensity profile intercepted by the receiver. Thus, both works handles the same design method by different but analogous approaches.

Other works have optimized secondary optics using search algorithms coupled with Monte Carlo Ray-Tracing (MCRT) simulations [28–32] to determine the decision variables that yield the highest performance.

Cheng et al. [28] have used Particle Swarm Optimization (PSO) to find optimum geometric parameters of a CPC that maximizes an annual metric of optical efficiency of the LFC. Men et al. [29] optimized CPC secondaries through a multi-objective genetic algorithm search that accounts for optical efficiency and flux uniformity.

Ajdad et al. [30] studied the optimum geometric parameters of a secondary optic whose one symmetrical side is composed of a vertical parabola facing down the primary field – the Double Parabolic Concentrator (DPC) – by a PSO algorithm. Ahmadpour et al. [31] optimized the DPC by different computational intelligence methods to achieve the geometric settings that yield the highest daily average optical efficiency on a summer day in Ardabil (Iran). Beltagy [32] used univariate parametric analysis to evaluate the settings of decision variables of the DPC optic that would maximize its optical efficiency at normal incidence. In the end, the author found that a CPC achieves better results than the optimum DPC.

Recently, Souza et al. [33] extended the work of Gomes et al. [34] to propose the aplanatic LFC. This design comprises an Aplanatic Optic Concentrator (AOC) as the secondary optic and geometric parameters of the primary field. The authors evaluated the design space regarding aplanatic decision variables to achieve the geometric settings with the highest intercept factor (i.e., optical efficiency).

Although the literature comprises a fair number of different secondary optics and comparative analyses between some of them were presented, it is still possible to identify open subjects that need further discussion.

Literature results indicate that TSC, PWC, SPC, and DPC secondaries fall compared to the CPC and ASC optics, whether in optical efficiency or flux homogeneity. Vouros' design [27] is analogous to the ASC proposed by Zhu [23], and other studies [24,25] highlight that CPC and ASC secondaries have practically the same profiles and the same performance. All of these proposed secondary optics add decision variables to the optimum design problem of LFCs, and an optimum set needs to be found to evaluate them properly – the exceptions are designs following the edge-rays principle for CPC and CEC.

In this sense, the CPC stands as the main secondary optic design. Optimum CPC geometries were determined by search heuristics [28,29], which does not necessarily obey the edge-ray principle. On the other hand, not using this principle implies adding more decision variables to the optimum design problem. Furthermore, the AOC and CEC designs were never compared to it. The SMS optic can be discarded since it accomplishes a very distinct design for the primary field.

Regarding to the comparison metrics, annual metrics of some studies [25,28,29] are surrogated models that consider the average of some representative days, instead of the distribution of incidences throughout the whole year. Other works [30,31] are based on daily averages.

Although optical efficiency is an important performance metric, low circumferential flux homogeneity is an issue in real operation since it can cause the failure of evacuated tubes, damaging the vacuum seal and leading to higher thermal losses. Results of previous works indicate a trade-off between efficiency and flux uniformity [7,25,29]. A more homogeneous flux distribution can also be achieved by a more suitable aim line than the absorber center [7,35]. Nevertheless, these previous comparison studies [7,25,29] did not comprise acceptance results, a key metric to assess the influence of different secondary optics on the concentrator tolerance to optical errors [18].

Considering the above discussion, the following research questions are proposed to be addressed in this work:

- How far are CPC and CEC edge-ray secondaries to the optimized CPC cases reported in the literature?
- How far are CPC and CEC edge-ray secondaries to the AOC?

To answer these questions, this work presents a comparison study based on annual average metrics of optical efficiency, flux uniformity, and acceptance, outputs of ray-tracing simulations and typical meteorological year hourly data. Thus, it is structured as follows. Section 2 presents the design of the analyzed secondary optics, as well as the main geometric model for the linear Fresnel concentrator. Then, Section 3 defines the analysis methods, comparison metrics, and approaches used throughout the study. Section 4 presents and discusses the results regarding the comparison of the different secondary optics. Finally, Section 5 presents conclusions and perspectives for future research activities.

2. Analyzed secondary optics

2.1. Geometric model

Fig. 1 illustrates the basic geometric model of a linear Fresnel collector with a single encapsulated absorber tube used throughout this work. It presents the primary field of reflectors in a horizontal position, where its edge points are marked as $\mathbf{F}_1$ and $\mathbf{F}_2$, so that the width of the primary field is represented by W_p. The absorber tube (the red circle), whose radius is denominated by r_a, can be encapsulated by a concentric glass cover (the blue circle) whose outer radius is given by r_{go}.

Fig. 1 shows that the absorber tube is located above the primary field at a particular height, here denominated by H_R. Usually, the center of the absorber defines the symmetry line of the concentrator, such that mirrors in the left side are equal to mirrors on the right side. Furthermore, this figure also shows the three geometric parameters related to the primary mirrors: w, d, and R, which stands for the width, the distance (the shift, or pitch) between neighboring mirrors, and the cylindrical curvature radius, respectively. Lastly, a length in the longitudinal plane is always considered to define the spatial geometry.

As shown in previous studies, parabolic and cylindrical primary mirrors are indistinguishable from the receiver perspective for a broad range of geometric conditions regarding the linear Fresnel collector [36]. Thus, here only cylindrical mirrors are addressed, which are

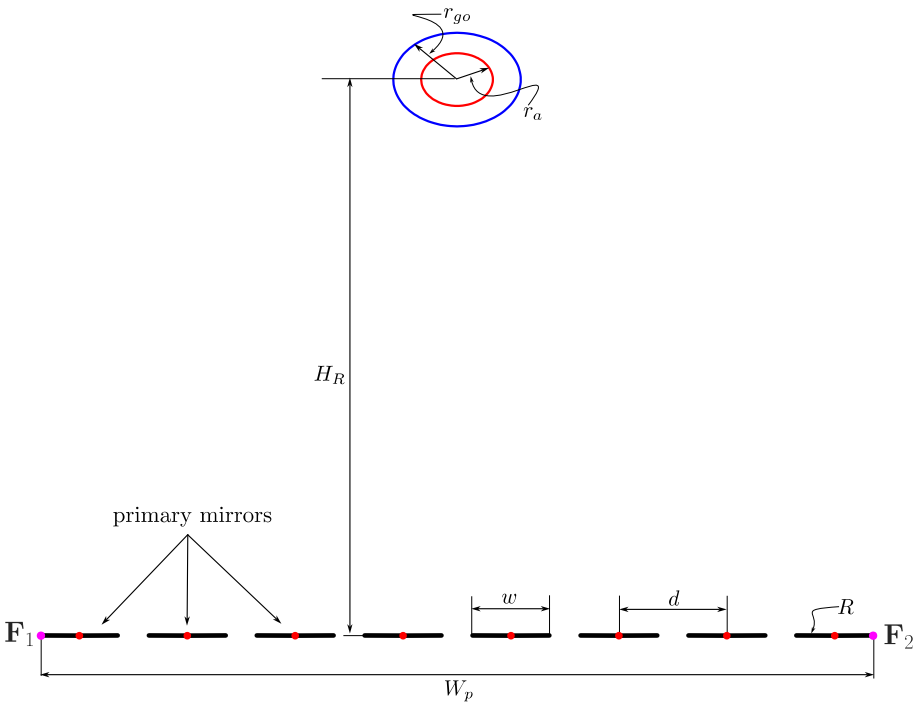

Fig. 1. Basic geometric model for a linear Fresnel Collectors with a single encapsulated absorber tube. The figure illustrates a transversal plane of the concentrator with the corresponding geometric parameters. The absorber tube (the red circle) radius is represented by r_a, whilst the outer radius of the concentric cover (the blue circle) is represented by r_{go}, which are located at a height H_R above the primary mirrors. The primary field is composed of N_m mirrors, has edge-points in $\mathbf{F}_1$ and $\mathbf{F}_2$, and comprises a total width given by W_p. Primary mirrors width and curvature radius are given by w and R, respectively, and the distance between (the center of) two neighboring mirrors is represented by d. (For interpretation of the references to colour in this figure legend, the reader is referred to the web version of this article.)

essentially equivalent to parabolic mirrors, where the curvature radii of the former are twice the focal lengths of the later: $R = 2f$, where f stands for the parabola focal length.

2.2. Non-imaging optic designs

Non-Imaging Optics (NIO) designs have been widely used as secondary optics for linear Fresnel collectors [5,20,22]. In general, these designs are based on the edge-ray principle, which states that if rays from the edges of the source (the primary field) are reflected onto the edges of the receiver (the absorber tube), all other in between rays will also reach the receiver [14,18].

Fig. 2 illustrates the edge-ray design of the Compound Parabolic Concentrator (CPC) and the Compound Elliptical Concentrator (CEC) as secondary optics for a Linear Fresnel Collector (LFC) with a single absorber tube – fundamentally, these optics are defined by the edge-rays (green lines) from the primary edges, $\mathbf{F}_1$ and $\mathbf{F}_2$, to the absorber edges, the tangent points $\mathbf{T}_1$ and $\mathbf{T}_2$, as shown Fig. 2a.

As shown in Fig. 2b, an edge-ray secondary optic is composed of involute and conic sections. A macro focal parabola is the conic of a CPC secondary, whilst a macro focal ellipse is the conic of a CEC optic.

The CPC design is fully defined by the absorber tube radius, r_a, the

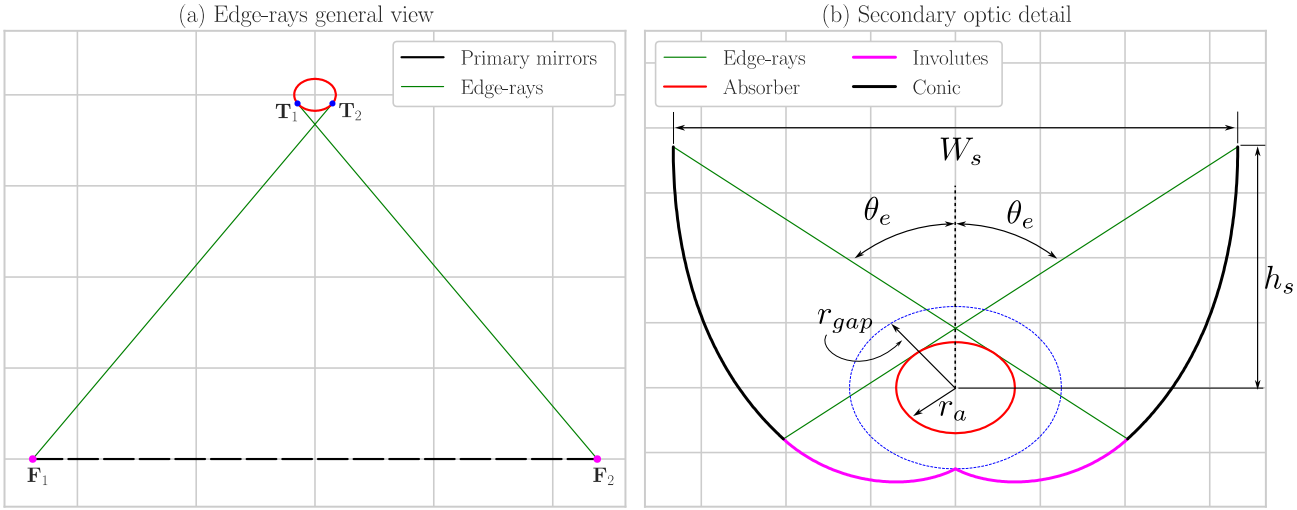

Fig. 2. Non-Imaging Optics (NIO) designs as the secondary optics of a Linear Fresnel Collector (LFC) with a tubular absorber. It shows (a) the edge-ray principle: rays from the edges of the primary field, $\mathbf{F}_1$ and $\mathbf{F}_2$, to the edges of the absorber tube, the tangent points $\mathbf{T}_1$ and $\mathbf{T}_2$; and (b) details regarding of the secondary optic: a macro focal parabola is the conic of a CPC secondary, whilst a macro focal ellipse if the conic of a CEC optic.

gap size, r_{gap}, and the angular aperture defined by the edge-rays, θ_e, which becomes its acceptance half-angle – thus, the secondary mirror reflects tangentially to the receiver, all rays that are parallel to the edge rays so defined, i.e., the primary field is modeled as an infinitely large source at an infinite distance. In the case of a CEC optic, the design is fully defined by r_a, r_{gap}, and the edge-points of the primary field, $\mathbf{F}_1$ and $\mathbf{F}_2$ – thus, it models the primary as a finite source at a finite distance, and all rays leaving $\mathbf{F}_1$ and $\mathbf{F}_2$ will reflect tangentially to the absorber [18]. Here, equations for involute and corresponding conics of CPC and CEC optics are not shown to present a more clean and concise text. However, these equations, as well as the design procedure, are detailed by Winston [17] and Chaves [18].

Fig. 2b shows an important geometric parameter: r_{gap}, the gap size (or gap radius). In theory, both CPC and CEC optics can be designed to touch the tube, i.e., $r_{gap} = 0$. However, to avoid thermal short-circuits (the absorber heats up) and due to practical conditions of an absorber with a glass cover, a gap is imposed between the secondary optic and the tube: $r_{gap} \geq r_{go} > r_a$. Alternatively, one can define $\Delta r_g = r_{gap} - r_{go}$ to rule the gap size. Of course, higher gaps mean more optical losses, so that a simple choice is to consider the lowest possible value: $\Delta r_g = 0$.

Oommen and Jayaraman [15] presented a set of simple equations for the CPC optic, functions of r_a, r_{gap}, and the acceptance half-angle, θ_a. Although this model was not presented as a secondary optic design for an LFC, many studies have used it with this purpose [24,25,28,29,32,35,37,38].

In this sense, Oommen's model [15] was used considering θ_a, r_{gap}, and a third parameter, the maximum opening angle, hereafter referred to as θ_{max}, as decision variables to be optimized [28,29]. That is, this design does not necessarily follow the edge-ray principle: the value of θ_a may differ from that of θ_e, with θ_{max} representing a measure for the truncation of the CPC optic – in a non-truncated case (full open optic), $\theta_a + \theta_{max} = 270°$.

Fig. 3 presents a validation of the implemented models for these non-imaging optic designs. Fig. 3a shows Oommen's model [15] by reproducing the geometry reported by Qiu et al. [38], where $r_a = 0.035$ m, $H_R = 8.0$ m, $r_{gap} = 0.0625$ m, $\theta_a = 56°$, and $\theta_{max} = 193.09°$ (3.37 rad) – as can be seen, the implemented functions yield an optic with $W_s = 0.295$ m and $h_s = 0.07$ m, which match the reported data. Furthermore, Fig. 3b shows a comparison of Chaves's [18] and Oommen's models [15] for the same design conditions, where $r_a = 0.035$ m, $r_{gap} = 0.0625$ m, $\theta_a = \theta_e = 60°$, and a full opened optic, i.e., $\theta_a + \theta_{max} = 270°$ $(3\pi/2)$ – as seen, both models yield the same contour.

2.3. Aplanatic design

Gomes et al. [34] have analyzed a fair range of the linear aplanatic design parameters (s, k, and, NA) that yield higher efficiency (intercept factor). Then, Souza et al. [33] extended this previous analysis to propose an aplanat linear Fresnel geometry with high concentration and high optical efficiency (intercept factor): the authors found that the optimum aplanat decision variables are $\{s,k,\text{NA}\} = \{-2.25,-0.1,1.0\}$, considering an absorber tube of $r_a = 0.012$ m, and primary aplanatic optic with a total aperture, W_a, of 1.9925 m – these aplanat primary and secondary optics are illustrated in Fig. 4a.

The determination of the linear Fresnel primary field from these primary and secondary aplanat optics is as follows. First, the aplanat primary is divided into twelve equal-width segments at the aperture plane. The center of each segment (depicted as blue dots in Fig. 4a) corresponds to a point in the aplanat secondary, as defined by the aplanat equations [34]. Next, center of each segment is projected onto a horizontal plane while maintaining the direction of the line connecting them to their corresponding point in the aplanat secondary – these points in the secondary serve as the tracking points for the primary mirrors, as illustrated in Fig. 4b. The green lines connect the center of the primary mirrors to the corresponding tracking points at the aplanat secondary optic. Although the primary mirrors are very close in Fig. 4a, a verification was done: the distance between two neighboring mirrors is enough for them not to collide in their tracking procedure. Finally, the curvature radius of each primary is defined by a zenithal reference design [39], which assumes normal incidence as the design position.

This process of constructing a segmented and horizontal linear Fresnel primary field from a continuous aplanat primary optic yields a uniform configuration in terms of width (meaning all primaries have the same width) but a non-uniform configuration in terms of curvature radius and distance between neighboring mirrors (each primary having its specific values).

3. Materials and methods

3.1. Overview

Ray-tracing is the most appropriate optical method for evaluating LFCs with a secondary optic since it can account for the complex optical phenomena (multiple reflections and transmission, as well as total internal reflection) that might occur in the receiver. In this work, ray-tracing simulations are carried out with SolTrace [40], and a Python

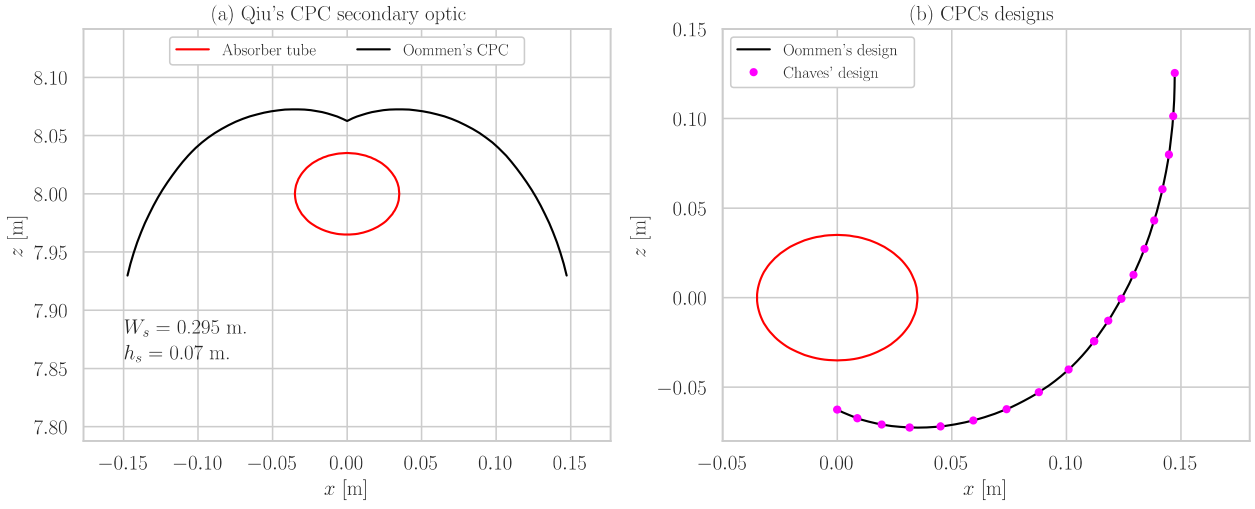

Fig. 3. Validation analysis regarding the implemented models for non-imaging optic designs. Figure (a) shows a geometry based on the data reported by Qiu et al. [38] – it yields a CPC aperture width of 0.295 m and located 7.93 m above the primary field. Figure (b) compares the CPC designs presented by Chaves [18] and Oommen and Jayaraman [15].

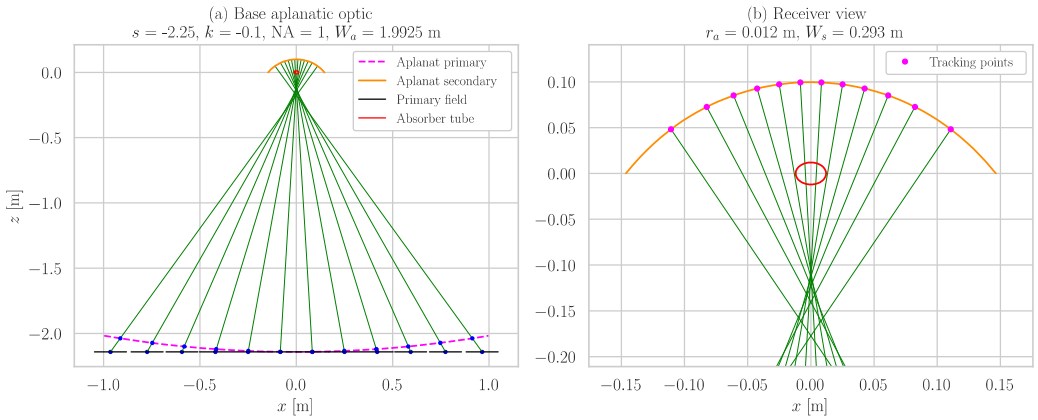

Fig. 4. The aplanat linear Fresnel concentrator proposed by Souza et al. [33]. Figure (a) shows primary and secondary aplanats for $\{s,k,\text{NA}\} = \{-2.25,-0.1,1.0\}$, and a primary width $W_a = 1.9925$ m, as well as the horizontal primary field constructed from the aplanat optics – the width of the primary field is larger than the value of the aplanat primary. Figure (b) shows a close look at the receiver and illustrates the tracking points of the primary mirrors.

library is used for automating script writing [41].

A transversal plane (bi-dimensional) model is considered. That is, the longitudinal effects are neglected, and a range of transversal incidence angles, θ_T, is considered in the optical characterization. In this sense, $\theta_T \in [0°, 85°]$ since only symmetric cases are addressed.

This optical characterization determines three performance metrics as functions of θ_T: optical efficiency, flux uniformity, and acceptance. The first one gives the conversion rate of incident sunlight into absorbed flux; the second represents an issue in real operation since low uniformity can cause the failure of evacuated tubes, damaging the vacuum seal and leading to higher thermal losses. The acceptance gives a metric of the concentrator tolerance to optical errors such as tracking and misalignments, an important factor in long-term energy collection, operation, and maintenance. Instantaneous and averaged metrics are defined in Section 3.2.

Moreover, annual average values of these metrics are calculated based on hourly data of a Typical Meteorological Year (TMY) taken from the PVGIS Application Program Interface [42]. For each one of the 8760 h of the year, sun azimuth and zenith are calculated by a solar position algorithm [43] and then converted to transversal and longitudinal incidence angles, θ_T and θ_L, respectively, considering North-South (NS) and East-West (EW) orientations for the concentrator.

3.2. Evaluation metrics

The optical efficiency, η, is defined as shown in Eq. (1), where Q_{abs} is the flux absorbed in the receiver, defined as the product between the number of absorbed rays, n^a_{rays}, and the power carried by each ray, q_{ray}, outputs of a ray-tracing simulation; I_b is the Direct Normal Irradiance (DNI), always considered as 1000 W/m^2, and A_{net} is the mirror aperture area (the sum of the product between mirror width, w, and length, L).

$$\eta = \frac{Q_{abs}}{I_b \cdot A_{net}} = \frac{q_{ray} \cdot n^a_{rays}}{I_b \cdot \sum w \cdot L} \tag{1}$$

Of course, η is a function of θ_T and one can write $\eta = \eta(\theta_T)$. Thus, an annual averaged value of efficiency, $\overline{\eta}$, is defined in Eq. (2), where h is an index that ranges for each of the 8760 h of the year.

$$\overline{\eta} = \frac{\sum_{h=1}^{8760} \eta(\theta^h_T) \cdot I^h_b \cdot A_{net}}{\sum_{h=1}^{8760} I^h_b \cdot A_{net}} \tag{2}$$

The circumferential flux uniformity is measured by the non-uniformity index, represented by δ, as defined in Eq. (3): higher values of δ_q mean lower flux uniformity, and vice-versa.

$$\delta_q = \frac{\sigma_q}{\mu_q} \tag{3}$$

In Eq. (3), μ_q is the average flux density in the absorber, as given by Eq. (4): the ratio of the absorbed flux in the receiver, Q_{abs}, and absorber area, A_{abs}.

$$\mu_q = \frac{Q_{abs}}{A_{abs}} \tag{4}$$

Then, σ_q represents the standard deviation of the circumferential flux distribution. In SolTrace, the circumferential width of the absorber tube is divided into bins, here represented by N_{bins}, and σ_q is calculated by a discrete approach, as given by Eq. (5), where q_i represents the flux density in a circumferential bin of index i.

$$\sigma_q = \sqrt{\frac{1}{N_{bins}} \sum_{i=1}^{N_{bins}} (q_i - \mu_q)^2} \tag{5}$$

In this work, $N_{bins} = 150$ for all simulations. In fact, q_i represents the average of the longitudinal bins: $q_i = \frac{1}{N_{y\text{-}bins}} \sum_{j=1}^{N_{y\text{-}bins}} q_{ij}$ where y refers to the direction of the longitudinal width of the absorber tube (divided in $N_{y\text{-}bins}$), and q_{ij} is the flux intensity in a bin of index ij. In this work, $N_{y\text{-}bins} = 150$ for all simulations.

Of course, δ is a function of θ_T and one can write $\delta_q = \delta_q(\theta_T)$. Thus, an annual averaged value of non-uniformity index, $\overline{\delta}_q$, is defined in Eq. (6), where h is an index that ranges for each of the 8760 h of the year.

$$\overline{\delta}_q = \frac{\sum_{h=1}^{8760} \delta_q(\theta^h_T) \cdot I^h_b \cdot A_{net}}{\sum_{h=1}^{8760} I^h_b \cdot A_{net}} \tag{6}$$

The acceptance of a linear Fresnel collector, as in non-ideal concentrators, is not based on geometric relations but on ray-tracing analysis since the transmission-acceptance curve does not follow the step-shaped function of ideal concentrators [18].

Thus, the acceptance half-angle, β, is calculated based on the off-axis incidence, here denominated by ψ, for which the concentrator collects 90 % of the on-axis flux [18]. Hence, the primary field is positioned for a particular transversal incidence θ_T, and then the absorbed flux is calculated for off-axis incidences ($\theta_T \pm \psi$) but without further tracking, as illustrated in Fig. 5a.

The off-axis incidences for which the absorbed flux is 90 % of the on-axis flux ($\psi = 0$) are ψ^+ and ψ^-, as shown in Fig. 5b. Therefore, β is calculated as given by Eq. (7).

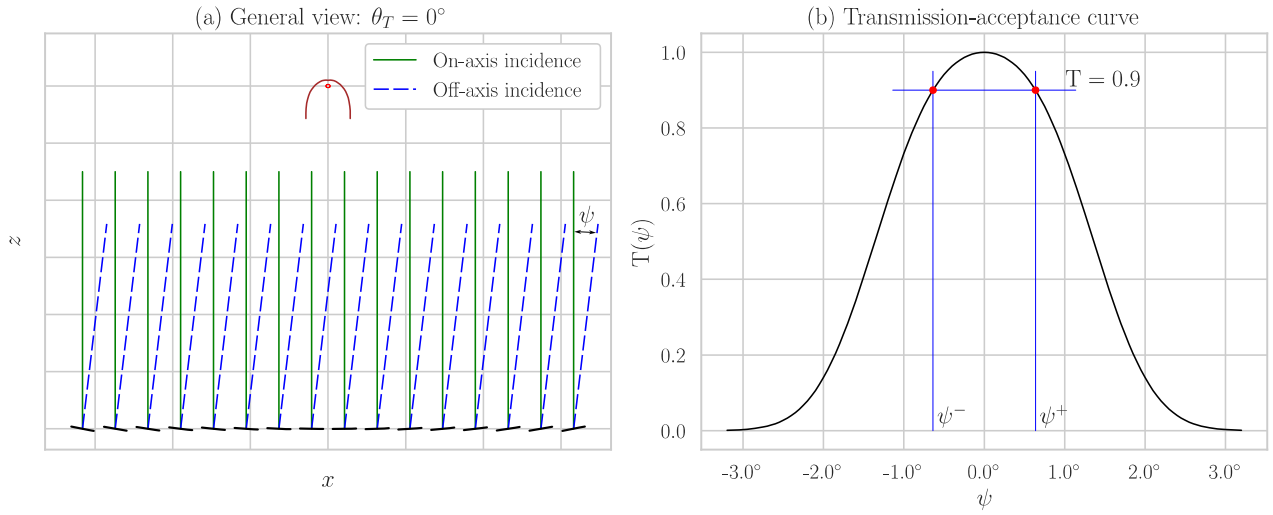

Fig. 5. Acceptance analysis for a Linear Fresnel Collector (LFC). Figure (a) illustrates the primary field positioned for a particular transversal incidence ($\theta_T = 0$), as well as the on-axis (green lines) and off-axis rays (dashed blue lines) for that position. Figure (b) shows the transmission-acceptance curve, i.e., how the normalized flux, T, varies with the off-axis incidence, ψ – the positive and negative off-axis incidences for which $T(\psi) = 0.9$ are ψ^+ and ψ^-, respectively. (For interpretation of the references to colour in this figure legend, the reader is referred to the web version of this article.)

$$\beta = \frac{\psi^+ - \psi^-}{2} \tag{7}$$

Of course, β is a function of θ_T and one can write $\beta = \beta(\theta_T)$. Thus, an annual averaged value of acceptance, $\overline{\beta}$, is defined in Eq. (8), where h is an index that ranges for each of the 8760 h of the year.

$$\overline{\beta} = \frac{\sum_{h=1}^{8760} \beta(\theta_T^h) \cdot I_b^h \cdot A_{net}}{\sum_{h=1}^{8760} I_b^h \cdot A_{net}} \tag{8}$$

3.3. Convergence analysis of traced rays

This section aims to determine the number of ray intersections to be traced to achieve convergence of the flux distributions. Thus, it was defined an LFC geometry with 132.8 m^2 of aperture area (16.56 m × 8.0 m) and a CEC secondary optic, as depicted in Table 1.

This convergence analysis of traced rays considers the settings presented in Table 2, where Δ_{sun} stands for the half-width of a pillbox sunshape. ρ_p and ρ_s refers to the reflectivity of primary and secondary optics, respectively. α and τ refers to the absorption of transmission coefficients of the absorber tube and glass cover, respectively. σ_{sp} and σ_s refers to the standard deviation of Gaussian profiles of the specular and slope errors, respectively.

Fig. 6 shows optical efficiency and circumferential uniformity index results for this convergence study. As can be seen, results converge very well for a number of intersections greater than 1.0×10^6. Moreover, the size of the 99 % confidence interval (three standard deviations) remains relatively constant beyond this value.

Therefore, based on the results shown in Fig. 6, a density of 9413 ray intersections per square meter of aperture area ($1.25 \times 10^6 \div 132.8$ m^2), and a seed number of 123 to ensure reproducibility, is then defined for all further simulations. Moreover, a minimum number of ray intersections of 2.0×10^5 is also considered to avoid simulations with very few rays.

Table 1
Linear Fresnel geometry used in convergence study. The primary field has a uniform width and shift, but a non-uniform curvature design (zenithal reference). The receiver comprises a SHOTT like evacuated tube, a CEC secondary optic, and glass cover thickness of 0.003 m.

N_m	W_p	w	d	R	r_a	r_{go}	r_{gap}	H_R
16	16.56	0.75	1.054	var*	0.035	0.0625	0.0625	7.2

*The curvature radius of the primary mirrors follows the zenithal reference design defined by Abbas and Martínez-Val [39]. Thus, the value is variable and depends on the mirror.

Table 2
Optical settings considered in the convergence analysis of traced rays.

ρ_p	ρ_s	α	τ	Δ_{sun}	σ_{sp}	σ_s
0.95	0.95	0.96	0.98	4.65	3.0	2.0

4. Results and discussion

4.1. Non-imaging optics secondaries

This section analyzes non-imaging designs proposed as secondary optics of the linear Fresnel solar concentrator. Thus, it compares CPC and CEC edge-ray designs [18] to geometries resulting from optimization routines that attribute decision variables to the secondary optic geometry that follows Oommen's formulation [15] of the CPC optic. Section 2.2 details the design of these optics.

Two optimization studies use the CPC optic geometry parameters as decision variables in the optimization routine: Cheng et al. [28] and Men et al. [29]. In the first study, particle swarm optimization was used to find the set of decision variables that maximizes a surrogated model of annual averaged optical efficiency; as for the last, a genetic algorithm was used as the search heuristic to determine the Pareto front of solutions which simultaneously maximizes surrogated models of annual efficiency and circumferential flux homogeneity – both studies consider the same optical properties, sunshape model, and optical errors, which are shown in Table 3.

The optimum geometry reported by Cheng et al. [28] for the case of a cylindrical primary field is hereafter denominated as Cheng's optic, and the corresponding geometric data is presented in Table 4. This geometry considers a distance between the absorber tube and outer cover radius of 0.0225 m. Therefore, $r_{gap} = r_a + 0.0225 + \Delta r_g$, where Δr_g was subjected to optimization within the range of $[0.01, 0.1]$ [28]. The reported value for r_{gap} by Cheng et al. [28] is not feasible since it would give Δr_g = -0.0125 m. Thus, a minimum value of gap size is here considered for Cheng's optic, i.e.,$\Delta r_g = 0.01$ m.

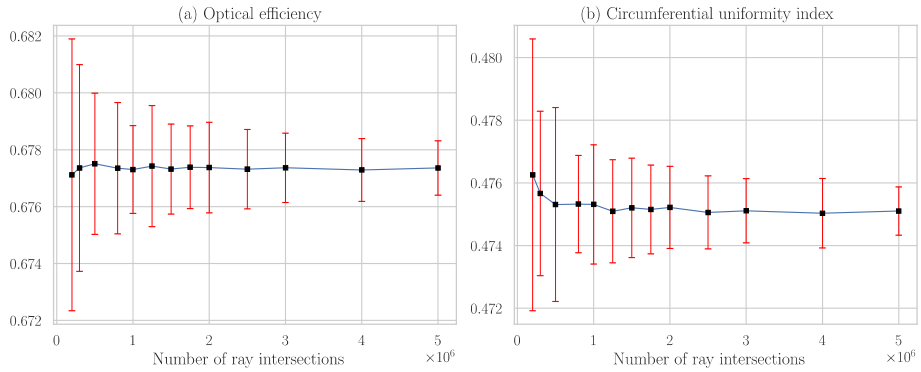

Fig. 6. Sensitivity analysis concerning the number of ray intersections to be traced. It shows how the results of the optical efficiency and circumferential uniformity index (both at normal incidence) vary in terms of the number of ray intersections. A total of 50 (fifty) simulations were carried out for each value of desired intersections so that the black squares represent the average value, and the red bars represent a 99 % confidence interval (±three standard deviations). All these ray-tracing simulations were carried out with the seed number in the trace configurations set as −1 to pseudorandom computation using the current CPU clock time. (For interpretation of the references to colour in this figure legend, the reader is referred to the web version of this article.)

Table 3
Optical settings considered by Cheng et al. [28] and Men et al. [29]. σ_t and σ_s refers to the standard deviation of Gaussian profiles of the tracking and slope errors, respectively. *The tracking error is only considered for the primary mirrors. †The slope error is considered for both primary and secondary reflectors.

ρ_p	ρ_s	α	τ	Δ_{sun}	σ_t*	σ_s †
0.92	0.95	0.96	0.95	4.65	0.5	2.5

Fig. 7 illustrates the Cheng's optic detailed in Table 4, and edge-ray designs of CPC and CEC optics are also shown in Fig. 7b – all secondary optics are designed with a minimum value for r_{gap}. $\Delta r_g = 0.01$ m is the lowest value considered by Cheng et al. [28]. Furthermore, the tracking point of each primary mirror is the center of the secondary optic aperture.

In Fig. 7b, the optimum geometry of the secondary optic reported by Cheng et al. [28] significantly deviates from the two edge-ray designs: CPC and CEC. Cheng's optic features a narrower aperture width and distinctly fails to align with the edge-rays originating from the primary field (green lines). Comparatively, the other two secondary optics – CPC and CEC – exhibit considerable similarity, differing mainly in their conic sections (macro focal parabola versus macro focal ellipse).

Fig. 8 presents the result of ray-tracing simulations for the optics depicted in Fig. 7. Cheng's optic demonstrates superior optical efficiency compared to the edge-ray designs, as shown in Fig. 8a. However, when evaluating circumferential flux uniformity and acceptance, Cheng's optic emerges as the least favorable design, as illustrated in Fig. 8b and Fig. 8c, respectively. These performance variations are consistent across the entire range of transversal incidences. It is worth noting that Cheng's optic was optimized solely to maximize annual efficiency and did not consider any other objectives.

Fig. 9 presents the annual averaged values of the three metrics presented in Fig. 8, showcasing CPC and CEC relative variations concerning Cheng's optic, with reference to TMY data from Jiexi County (N23.45°, E115.90°) [28]. The higher optical efficiency of Cheng's optic primarily stems from the shading caused by the receiver on the primary field: larger secondary optics, such as CEC and CPC, cast more shade for the same incidence angle. Another factor impacting efficiency relates to h_s (refer to Fig. 2), the height of the secondary optic: in Cheng's optic, more rays directly strike the absorber compared to the other two secondaries, as the aperture center is closer to the absorber, resulting in a lower average number of reflections. This phenomenon is evident in the circumferential flux uniformity, as depicted in Fig. 8b: Cheng's optic exhibits markedly inferior performance. Regarding acceptance, Cheng's optic fares poorly (as shown in Fig. 9), likely due to its smaller aperture size compared to the other two. However, aperture size alone does not entirely dictate acceptance results, as the differences between CPC and CEC are not as significant (as seen in Fig. 7b), yet their acceptances vary (as shown in Fig. 9). Thus, the match of the secondary optic profile with the primary optic also plays a crucial role in determining acceptance results.

The study conducted by Men et al. [29] is a multi-objective optimization aiming to simultaneously maximize annual surrogated models of optical efficiency and circumferential flux homogeneity. Consequently, the Pareto front of solutions was determined – the Pareto front represents the trade-offs between the different objectives, where improving one objective can only be achieved at the expense of worsening at least one other objective. Then, the TOPSIS algorithm was used to select a set of 36 recommended geometries from the Pareto solutions. These recommended solutions are henceforth referred to as Men's optic, followed by the corresponding index number from the original work. For example, Men's optic #1 denotes the recommended solution indexed as 1 in the research conducted by Men et al. [29].

Upon an initial analysis of these recommended geometries, it becomes clear that all of them refers to non-truncated CPC optics, given that $\theta_a + \theta_{max} = 270°$ for all cases. Among these recommended geometries, Men's optic #31 exhibits the highest disparity between edge-rays aperture angle and the CPC acceptance angle, θ_e and θ_a, respectively (see Fig. 2): $\theta_a - \theta_e = 7.71°$. However, it is worth noting that this geometry is optimized for a location with a latitude of 75°, which lacks practical relevance. Therefore, for the purpose of this discussion, it is only considered locations with a latitude lower or equal than 45°.

In this sense, Men's optic #15 is the one which shows the higher deviation: $\theta_a - \theta_e = 6.27°$. Its corresponding geometric data is presented in Table 5. In this case, a distance between absorber and outer cover radius of 0.0225 m, so that $r_{gap} = r_a + 0.0225 + \Delta r_g$, where Δr_g

Table 4
Geometric parameters of the optimum configuration reported by Cheng et al. [28], henceforth referred to as Cheng's optic. It was considered a glass cover thickness of 0.003 m.

N_m	W_p	w	d	R	r_a	r_{go}	r_{gap}	H_R	θ_a	θ_{max}
25	12.25	0.25	0.50	24.75	0.1	0.1225	0.1325	9.49	66.29°	183.69°

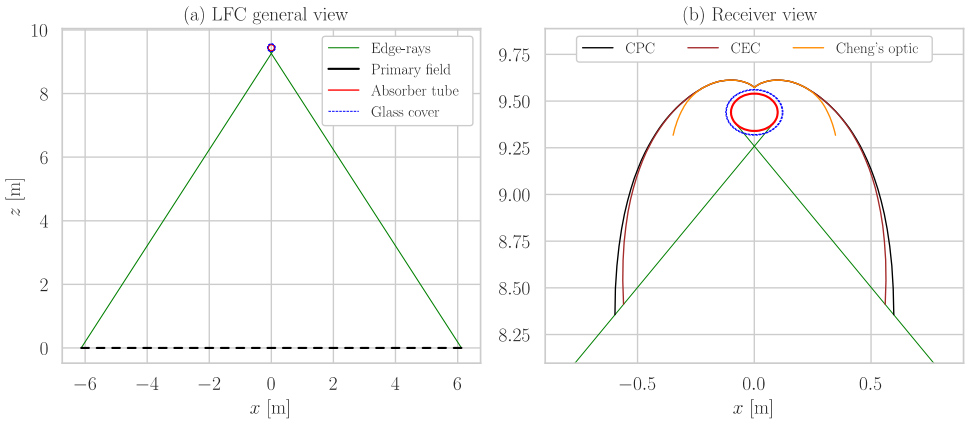

Fig. 7. Linear Fresnel Collector optimum geometry reported by Cheng et al. [28] (see Table 4). It illustrates (a) the general view of the primary field, absorber tube, glass cover, and edge-rays – the primary field has a uniform configuration and is shown at a horizontal position; (b) a close look at the receiver, with different secondary optics designs: CPC and CEC relate to edge-rays designs defined in Section 2.2, and Cheng's optic refers the reported optimum geometry.

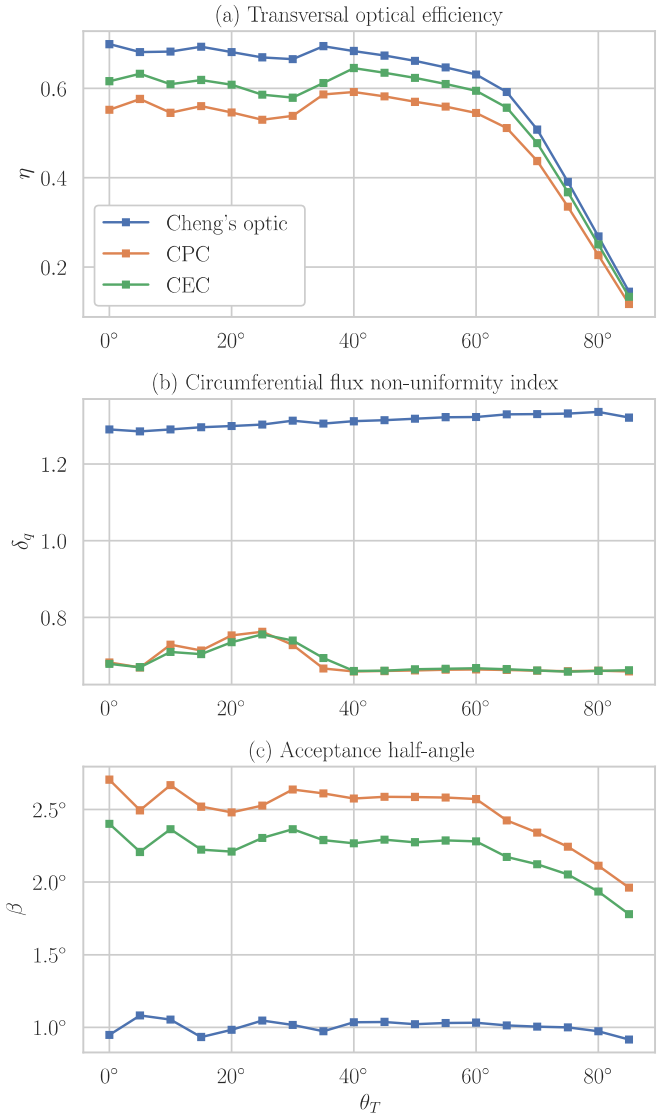

Fig. 8. Results of (a) Transversal optical efficiency, (b) Circumferential uniformity index, and (c) Acceptance half-angle as functions of θ_T, the transversal incidence angle, for Cheng's optic and corresponding CPC and CEC edge-ray secondary optics (see Fig. 7). The optimum geometry reported by Cheng et al. [28] is denominated as Cheng's optic (see Table 4).

was optimized within the range of $[0.01, 0.1]$ [29].

In Fig. 10a, CPC and CEC secondary optics designed for Men's optic #15, based on the edge-rays principle, are also depicted. These two optics adhere to the minimum gap size: $r_{gap} = 0.0825$ m, meaning $\Delta r_g = 0.01$ m, which is the smallest value considered by Men et al. [29]. For this condition, interestingly, CPC and CEC edge-ray geometries essentially overlap and closely resemble each other. However, it's evident that Men's optic #15 does not match with the edge rays from the primary field, as illustrated in Fig. 10a.

Fig. 11 presents ray-tracing results for the optics in Fig. 10a. The performance of CPC and CEC largely overlaps, aligning with expectations from their contour (refer to Fig. 10b). Both of these optics outperform Men's optic #15 in terms of efficiency and acceptance results, although they are surpassed in flux uniformity.

In Fig. 12, CPC and CEC annual average values of optical efficiency, non-uniformity index, and acceptance half-angle are presented as relative variations with respect to Men's optic #15. These calculations are conducted considering the TMY data from Evora (N38.53°, W8.00°) and the optical characterization data in Fig. 11.

In Fig. 12, variations are not high as in the previous case (refer to Fig. 9), aligning with the closer profiles shown in Fig. 10b. In this scenario, the edge-ray designs exhibit higher efficiency and acceptance but demonstrate lower performance in flux uniformity, as indicated by the higher non-uniformity index. On the one hand, CPC and CEC optics feature smaller values for secondary optic aperture and gap, which helps in reducing optical losses and enhancing efficiency. Conversely, the higher value of h_s (see Fig. 2) increases the average number of reflections and consequently reduces efficiency. Moreover, it becomes evident that the size of the secondary optic aperture has a lesser effect on acceptance compared to the optic profile: Men's optic #15 exhibits the lower average acceptance despite having the larger aperture. Additionally, while the gap size contributes to increased losses and reduced efficiency, it also contributes to improved flux uniformity.

In fact, when considering edge-ray designs with the same gap size as in Men's optic #15 (refer to Table 5), CPC and CEC optics align even more with it, as illustrated in Fig. 10b: geometry profiles are now even closer to each other.

Fig. 13 shows metrics average values for the optics illustrated in Fig. 10b. Efficiency and flux uniformity results are now closer. However, on the contrary, the acceptance differences are now more pronounced, driven by the larger apertures of the CPC and CEC secondaries compared to Men's optic #15 in addition to the already matching optic profile.

These previous finding highlight how edge-ray designs draw nearer to a Pareto solution of a bi-objective optimization problem considering a flux uniformity metric alongside an optical efficiency objective, as it can be seen from Cheng et al. [28] to Men et al. [29]. Indeed, the results in

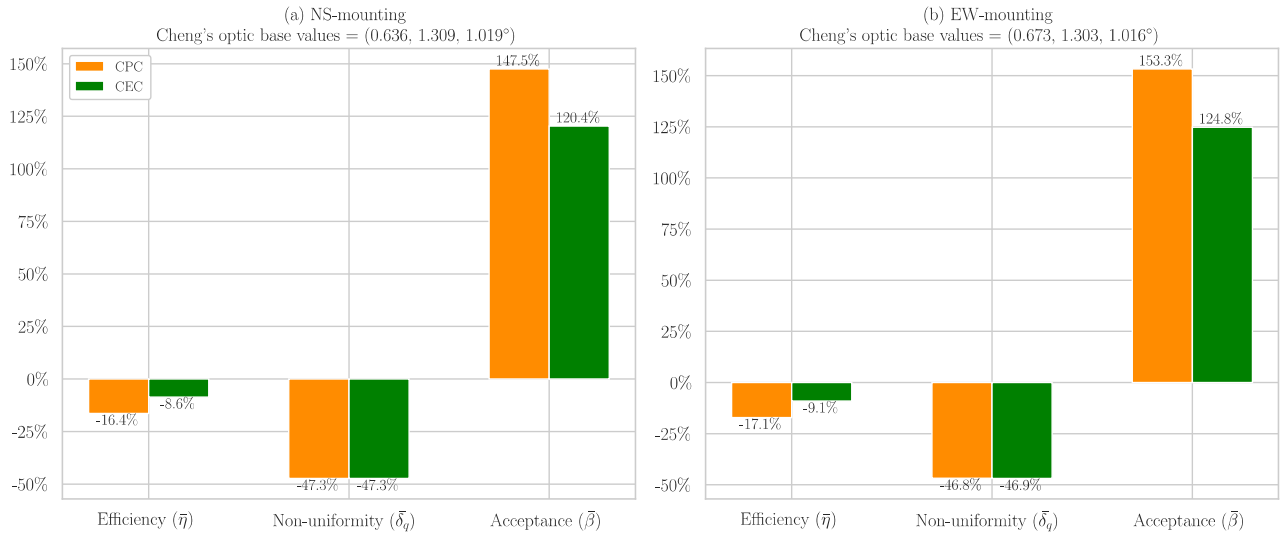

Fig. 9. Annual average values of optical efficiency, non-uniformity index, and acceptance half-angle of CPC and CEC secondary optics as the relative difference to Cheng's optic (see Fig. 7). Cheng's annual average metrics of efficiency, non-uniformity, and acceptance are (0.636, 1.309, 1.019°) and (0.673, 1.303, 1.016°) for NS and EW-mountings, respectively. Furthermore, it considers TMY data from Jiexi County (N23.45°, E115.90°) [28].

Table 5
Geometric parameters of an optimum configuration reported by Men et al. [29]. It shows the geometric parameters of recommended solution #15, denominated as Men's optic #15. A glass cover with a thickness of 0.003 m was considered.

N_m	W_p	w	d	R	r_a	r_{go}	r_{gap}	H_R	θ_a	θ_{max}	Latitude
25	31.43	0.71	1.28	47.14	0.05	0.0725	0.11	14.95	52.81°	217.19°	[30°,45°]

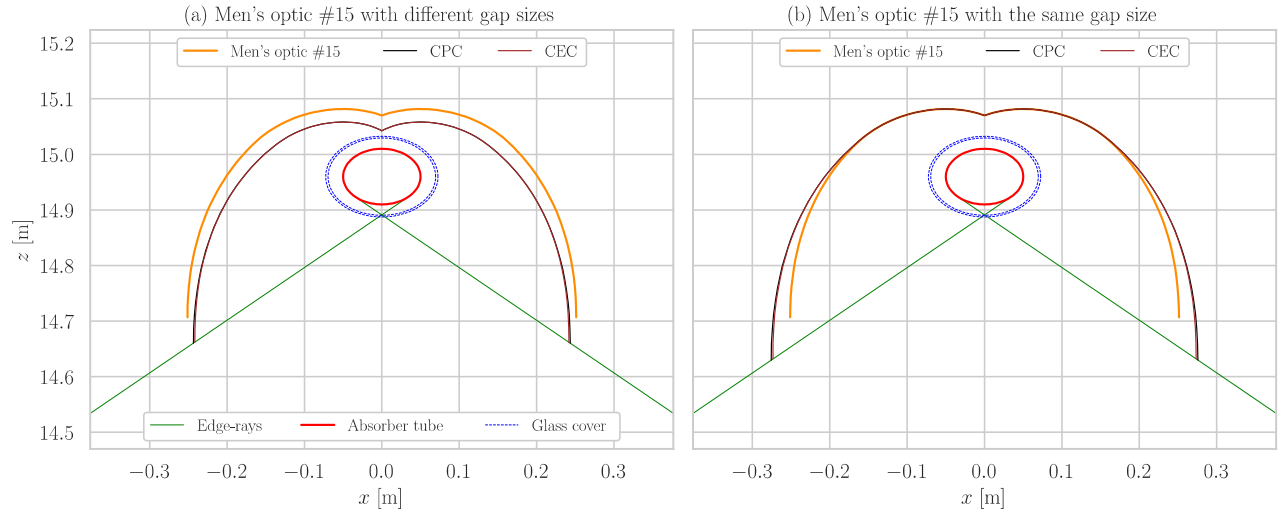

Fig. 10. Receiver details of different secondary optics for Men's optic #15 (see Table 5). In Figure (a), CPC and CEC edge-ray designs have the minimum possible gap size (r_{gap} = 0.0825 m), a value lower than of Men's optic #15 (r_{gap} = 0.11 m). In Figure (b), CPC and CEC edge-ray designs have the same gap size of Men's optic #15 (r_{gap} = 0.11 m).

Fig. 12 indicate that edge-ray designs are not dominated by Men's optic #15 (a Pareto solution) and can become even more closely aligned, as depicted in Fig. 13, when the same gap radius is used for all secondary optics. Furthermore, edge-ray designs offer an additional advantage in acceptance, signifying higher tolerance to optical errors.

An intriguing observation from analyzing Men's recommended solutions is that although geometric parameters of the primary field vary within a reasonable range, the corresponding CPC geometry does not significantly deviate from an edge-ray. The case with the highest deviation, Men's optic #15, was here analyzed, where $\theta_a - \theta_e = 6.27°$.

The case with the lowest difference is Men's optic #4, where $\theta_a - \theta_e = 0.46°$. Now, simulation results for the CPC edge-ray design and the reported optimum geometry practically overlap when they have the same r_{gap}, as shown in Fig. 14b. Thus, only the gap size, denoted by r_{gap}, emerges as an important decision variable in the edge-ray design to balance efficiency, flux uniformity, and acceptance – a higher gap means lower efficiency but higher values of circumferential uniformity and acceptance.

Furthermore, considering the optimal geometries reported by Cheng et al. [28] and Men et al. [29], the previous results indicate that non-truncated (full open) CPC optics play a crucial role in achieving higher

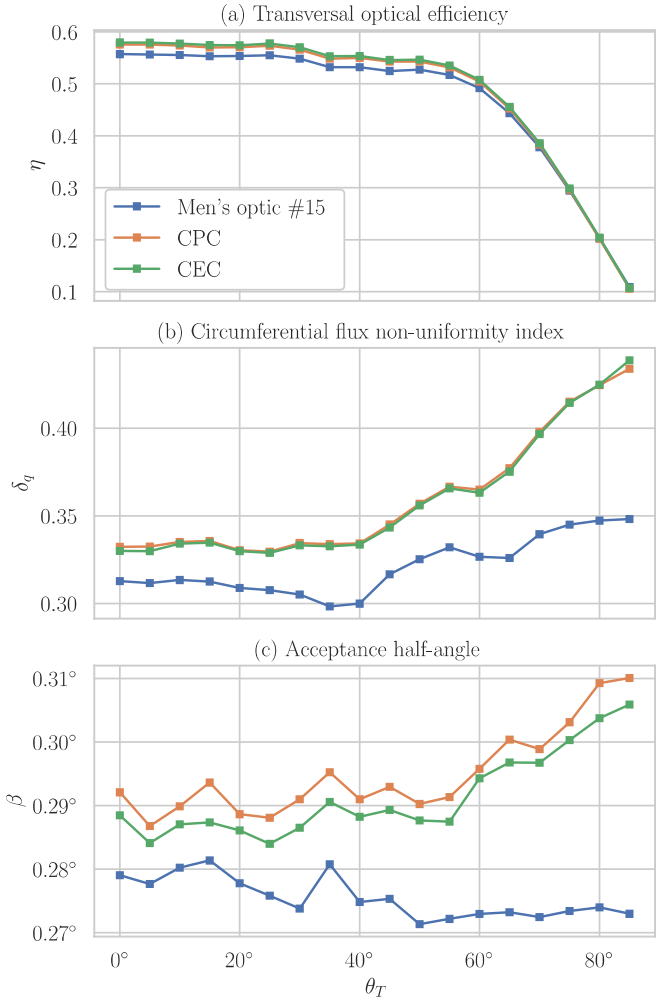

Fig. 11. Results of (a) Transversal optical efficiency, (b) Circumferential uniformity index, and (c) Acceptance half-angle as functions of θ_T, the transversal incidence angle, for Men's optic #15 and corresponding cases with CPC and CEC edge-ray secondary optics, considering that edge-ray designs have the minimum possible gap size, as shown in Fig. 10a.

levels of circumferential flux uniformity.

It is worth noting that the optimal geometries reported by Men et al. [29] comprise a subset of the Pareto front selected by the TOPSIS algorithm. Consequently, not all Pareto solutions were reported, implying that the CPC edge-ray designs might be part of the optimal solutions from the Pareto front but not selected by the TOPSIS.

4.2. Aplanat optic comparison

Considering the aplanat linear Fresnel geometry showed in Fig. 4, CPC and CEC edge-ray secondary optics were designed for a comparison analysis, as shown in Fig. 15. For this matter, a gap size was considered so that $r_{gap}/r_a = 1.786$ – the ratio of outer cover radius and absorber radius in standard PTR®70 evacuated tubes [10] and $\Delta r_g = 0$. However, to follow Souza et al. [33], a glass cover was not included in the simulations. The geometric data for the optics in Fig. 15 are shown in Table 6.

Fig. 15a shows a general view of the aplanat LFC, and the edge-rays from the primary field to the absorber tube. As detailed in Fig. 15b, the designed CPC and CEC optics are quite close, and both significantly diverge to the aplanat secondary. Moreover, the aplanat presents a larger aperture, as well as far bigger gap. It is important to highlight that whilst in CPC and CEC cases the tracking point is the secondary aperture center, the aplanat case has a specific tracking procedure, as shown previously discussed regarding Fig. 4.

Fig. 16 presents simulation results for the optics shown in Fig. 15. As seen, the CPC and CEC fairly surpass the aplanat optic in terms of acceptance for the whole range of θ_T, but the CEC is superior also in terms of efficiency. These results indicate that average values for different locations only impact the magnitude of the differences but not in determining which secondary optic is better. On the other hand, flux uniformity results show that the best optic depends on θ_T. Furthermore, the data on CPC and CEC follow previous results: the first outperforms the latter in acceptance, while it is surpassed in efficiency and present approximately the same flux uniformity results.

Fig. 17 displays the averaged values of the optical characterization data from Fig. 16, utilizing TMY data for Evora (N38.53°, W8.0°). It is evident that the CPC optic exhibits a slight disadvantage in efficiency compared to the Aplanat optic (3.0 % lower), while the CEC optical efficiency is nearly 8.0% higher. In this case of Evora, both CPC and CEC show higher levels of non-uniformity compared to the Aplanat, approximately 6.0% and 7.0%, respectively. Notably, both edge-rays optics demonstrate superior acceptance results, aligning with the finding from Fig. 16.

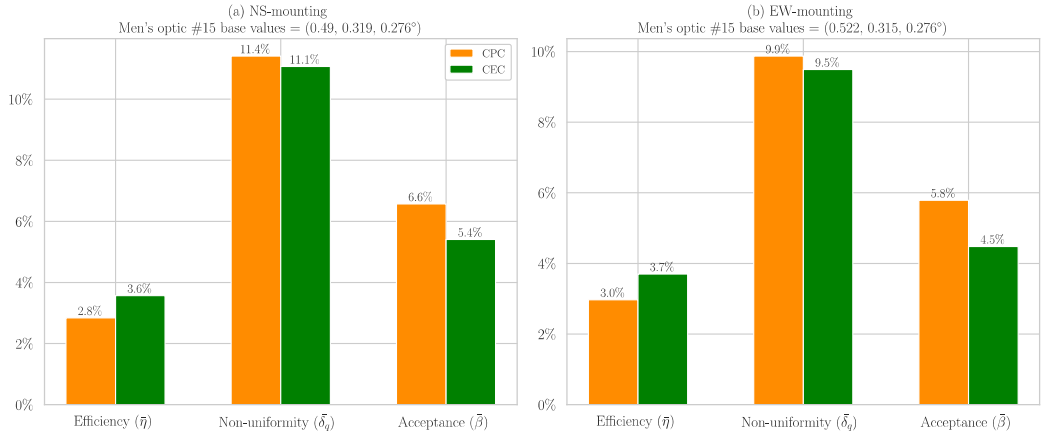

Fig. 12. Annual average values of optical efficiency, non-uniformity index, and acceptance half-angle of CPC and CEC secondary optics as the relative difference to Men's optic #15 (see Fig. 10a). It averages results from Fig. 11, considering the TMY data from Évora (N38.53°, W8.0°). Men's optic #15 annual average metrics of (efficiency, non-uniformity, and acceptance) are $(0.49,\ 0.319,\ 0.276°)$ and $(0.522, 0.315, 0.276°)$ for NS and EW-mountings, respectively, and are considered as the base values.

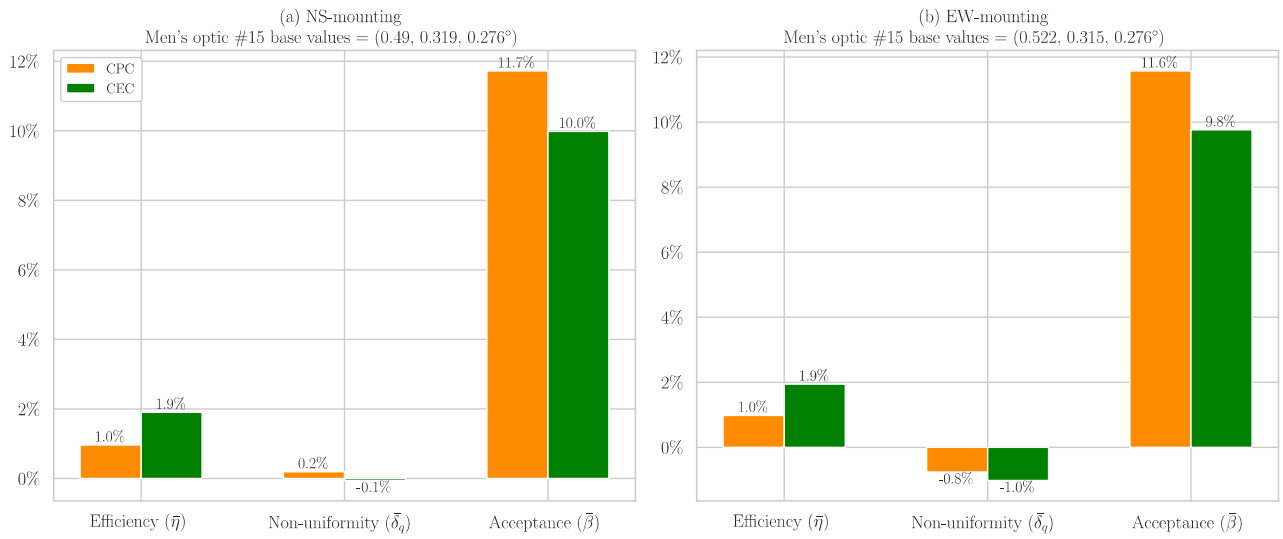

Fig. 13. Annual average values of optical efficiency, non-uniformity index, and acceptance half-angle of CPC and CEC secondary optics as the relative difference to Men's optic #15 when design with the same gap size: $r_{gap} = 0.11$ m (see Fig. 10b). It averages optical characterization results, considering the TMY data from Évora (N38.53°, W8.0°). Men's optic #15 annual average metrics of (efficiency, non-uniformity, and acceptance) are $(0.49,\ 0.319,\ 0.276°)$ and $(0.522,\ 0.315,\ 0.276°)$ for NS and EW-mountings, respectively, and are considered as the base values.

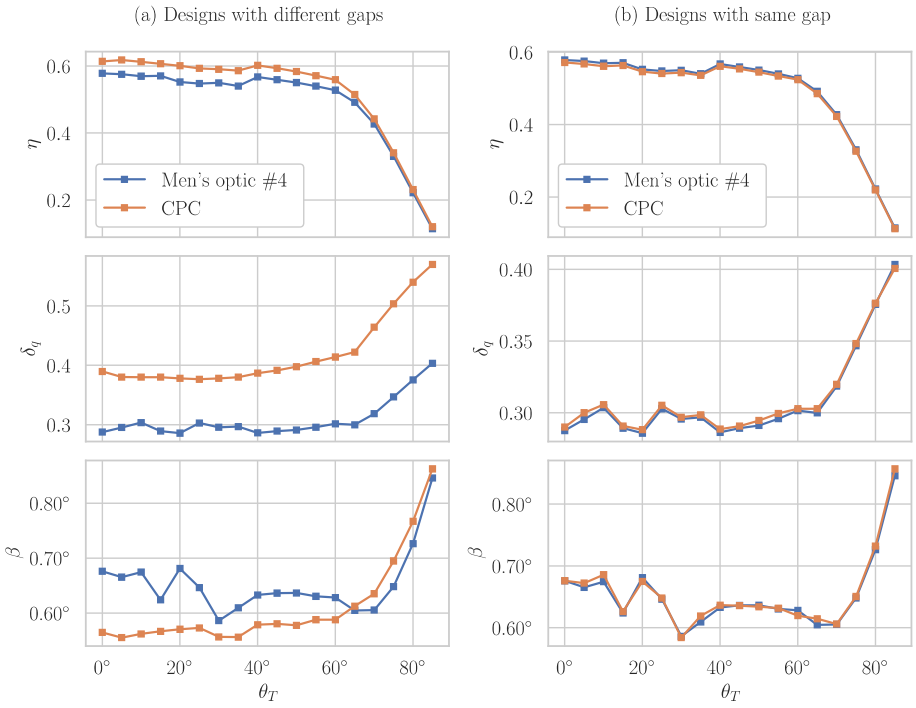

Fig. 14. A comparison of Men's optic #4 and CPC edge-ray design for (a) the minimum gap radius and (b) the condition of the same gap radius. It shows simulation results of transversal optical efficiency (η), Circumferential non-uniformity index (δ_q), and Acceptance half-angle (β) as functions of θ_T, the transversal incidence angle.

Hence, the results depicted in Fig. 17 shows that the aplanat optic generally surpasses edge-ray designs only in terms of flux uniformity. In this scenario the specific tracking procedure proposed by Souza et al. [33] aligns primary mirrors with the aplanat secondary optic, thereby ensuring that a larger portion of the absorber is illuminated. Qiu et al. [35] have demonstrated that employing a suitable aiming strategy can enhance flux uniformity without significantly sacrificing efficiency. Conversely, CPC and CEC edge-ray designs utilize the standard aiming strategy, complicating the illumination of the top of the absorber tube.

The evident advantage of CPC and CEC optics in acceptance implies a greater tolerance to optical errors, which is a crucial factor in long-run operation and maintenance of solar concentrators. Furthermore, it is worth noting that edge-ray designs require only a single decision variable to be determined – the gap size (or radius), denoted as r_{gap}. This can even be simplified by opting for the minimum feasible gap. Hence, edge-rays designs represents a more straightforward and simpler approach.

On the contrary, the aplanat linear Fresnel design analyzed here stems from a prior optimum search in the decision variable space involving s, k, and NA, as outlined by Souza et al. [33]. Consequently, any alteration in one parameter (e.g., the absorber tube radius) would

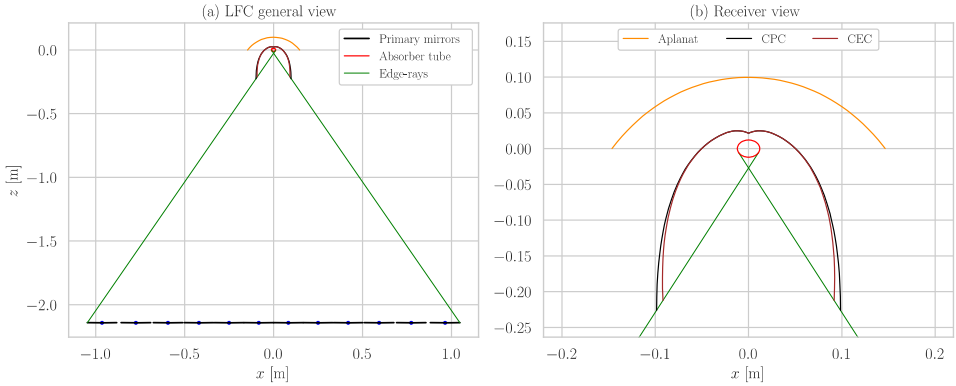

Fig. 15. A comparison of the aplanat linear Fresnel collector with CPC and CEC edge-ray secondary optics. It shows (a) the geometry general view and (b) the details of the receiver with the different secondary optics (CPC, CEC, and the aplanat secondary).

Table 6
Geometric data and optical properties of the aplanat linear Fresnel. σ_{sun} represents the standard deviation of a Gaussian sunshape, in mrad, as considered in the analysis carried out by Souza et al. [33].

N_m	W_p	w	d	R	r_a	r_{gap}	H_R	σ_{sun}	ρ_p	ρ_s	α
12	2.094	0.166	var*	var**	0.012	0.214	2.142	9.0	0.95	0.95	0.95

*The distance between the primary mirrors vary as given by the aplanat primary field design detailed in Section 2.3. ** The curvature radius of the primary mirrors follows the sun reference design proposed by Abbas and Martínez-Val [39] – thus, the value is variable and depends on the mirror.

lead to new optimum search for s, k, and NA, which is not the case with the edge-ray design method.

4.3. Further analysis on energy collection

The impact of a lower value of averaged annual efficiency, $\overline{\eta}$, on energy collection is direct since this metric represents how much of the incident energy is collected. However, flux non-uniformity, $\overline{\delta}_q$, and concentrator acceptance, $\overline{\beta}$, have impact on collector reliability and energy collection during long-term operation.

Issues with flux uniformity can result in thermal stress that damages absorbers and may even lead to the failure of evacuated tubes, compromising the vacuum seal and causing higher thermal losses. Additionally, the heat transfer fluid can only absorb a maximum flux density without deteriorating its properties. The concentrator acceptance plays a significant role as continuous and long-run operation introduces errors on the optical system.

While the impact of lower uniformity on energy collection is evident, accurately quantifying the value is challenging without reliable operational and maintenance models and a metric for circumferential uniformity as a safety benchmark. On the other hand, a straightforward analysis demonstrates how lower acceptance mean a decrease in energy collection.

The overall optical error is here denominated by σ_o, and is computed by the convolution of all errors [3]: ${\sigma_o}^2 = 4{\sigma_t}^2 + 4{\sigma_s}^2 + {\sigma_{sp}}^2$. The overall error (e.g., refer to Table 3 and Table 6) considered for performance computations is a kind of an idealization as it is constant and do not vary in time to capture the long-run operational issues, i.e., annual analyzes considers a fixed value of σ_o. The operation introduces errors beyond those gathered in σ_o due to further tracking deviations, soiling leading to more non-specular reflection, misalignments related to erection, mechanical bending, and wear, among other factors.

These additional errors are here represented by $\Delta\sigma_o$, and the final total optical error, σ_o^*, is then given by ${\sigma_o^*}^2 = {\sigma_o}^2 + \Delta{\sigma_o}^2$. Thus, $\Delta\sigma_o$ represents a measure of the deterioration of the optical system.

Fig. 18 shows the impact of $\Delta\sigma_o$ on the annual averaged efficiency, $\overline{\eta}$, as $\Delta\sigma_o$ varies up to 25 mrad, for Cheng and the Aplanat cases. Here, $\Delta\overline{\eta}$ stands for the relative difference of annual averaged efficiency of edge-rays designs to Cheng's (refer to Fig. 7) and the Aplanat (refer to Fig. 15) optics. Thus, for example, in Fig. 18a, for the CPC curve (in orange), $\Delta\overline{\eta} = (\overline{\eta}_{\text{CPC}} - \overline{\eta}_{\text{Cheng}})/\overline{\eta}_{\text{Cheng}}$.

Fig. 18a shows that as $\Delta\sigma_o$ increases, $\Delta\overline{\eta}$ drops. Thus, as expected, CPC and CEC edge-ray designs present a higher tolerance to errors. Indeed, as the additional error achieves a value of 15 mrad, the CEC design has the same efficiency as Cheng's optic – 20 mrad for the CPC design. For conditions beyond these values, edge-ray designs have a higher value of annual averaged efficiency the Cheng's optic ($\Delta\overline{\eta} > 0$).

In the case of Fig. 18b, the Aplanat comparison, $\Delta\overline{\eta}$ drops as $\Delta\sigma_o$ increases. However, the values of $\Delta\sigma_o$ for which $\Delta\overline{\eta} = 0$ are now different. Indeed, the CEC starts with a higher efficiency ($\Delta\overline{\eta} > 0$), as expected from the data in Fig. 17, and this difference increases with $\Delta\sigma_o$. For the CPC design, it has the same efficiency as the Aplanatic optic ($\Delta\overline{\eta} = 0$) at $\Delta\sigma_o = 5.0$ mrad, and higher efficiencies beyond it. These results agree with the data in Fig. 17: since the Aplanatic optic has a far lower acceptance than CPC and CEC designs, it experiences a more pronounced reduction in the efficiency as the optical errors conditions increases.

From another perspective, what do additional optical errors mean in real operating conditions? Specifically, how much operating time results in an additional error of 5.0 mrad on the tracking system? How many millimeters of misalignment in the receiver position correspond to an error of 20.0 mrad? Unfortunately, according to the authors knowledge, there are no studies that provide a general correlation between these factors.

On the other hand, it is possible to run further simulations to assess the relation between an error in the receiver position (in both x and z axes – refer to Fig. 7 and Fig. 15) to the corresponding variation of annual optical efficiency. The ensuing results of these simulations are presented in Fig. 19 for Cheng's and Aplanat comparisons. In Fig. 19a, in the case of the CEC curves (in green), $\Delta\overline{\eta} = (\overline{\eta}_{\text{CEC}} - \overline{\eta}_{\text{Cheng}})/\overline{\eta}_{\text{Cheng}}$.

In general, Fig. 19 shows that analyzed optics are far more sensitive to an error position in the x axis (horizontal) than in the z (vertical). In Fig. 19a, misalignments in the x axis of 0.2 m introduces losses such that the annual efficiency of the CEC becomes higher than that of Cheng's optic ($\Delta\overline{\eta} > 0$), and values higher than it are needed for the CPC to become more efficient than Cheng's optic – a corresponding error

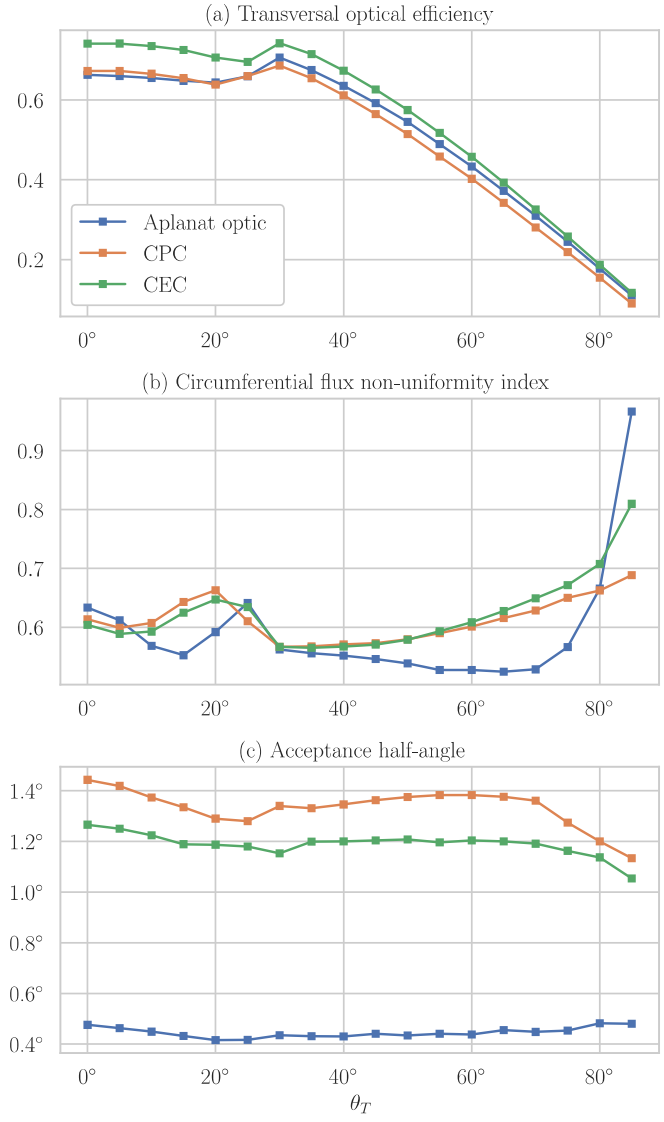

Fig. 16. Results of (a) Transversal optical efficiency, (b) Circumferential uniformity index, and (c) Acceptance half-angle as functions of θ_T, the transversal incidence angle. It considers the case reported by Souza et al. [33] and secondary optic edge-ray designs (CPC and CEC) for the reported optimum aplanat geometry.

position in the axis z does not produces the same effect. Conversely, an error position of 0.2 m does not seem a reasonable condition related to best practices of EPC (Engineering, Procurement, and Construction) companies.

In the case of the Aplanat comparison, Fig. 19b, the break-even values of error position ($\Delta\bar{\eta} = 0$) are significantly lower than that of Fig. 19a, where a misalignment in the axis x higher than 0.01 m turns the CPC into a more efficient optic than the Aplanat case – the CEC stars (error position of zero) being a more efficient case. Considering the error position in the z-axis, values above 0.04 m stablishes a conditions for which the CPC is more efficient than the Aplanat optic – these values are now closer to best practices of EPC companies.

In general, the results of this sections illustrate how the higher tolerance to optical errors of edge-rays designs have a further impact on collector reliability and energy collection during long-term operation. Furthermore, this higher tolerance to errors means that using cheaper materials and manufacturing methods does not significantly impact the performance of CPC and CEC edge-ray designs. Consequently, despite their lower efficiency, edge-ray designs might be more cost-effective solutions, i.e., have lower cost of generated energy. Unfortunately, to the best of the authors' knowledge, there are no studies that provide models to relate materials and manufacturing methods to a metric of the resulting optical errors and the concentrator cost, making this cost-energy assessment possible. Developing such models is, of course, beyond the scope of this paper.

5. Conclusions

This work analyzes secondary optics for Linear Fresnel Collectors (LFCs) with a single absorber tube, and shows comparison based on averaged annual metrics of optical efficiency, flux uniformity, and acceptance angle, outputs of ray-tracing simulations and typical meteorological year hourly data.

The literature review indicates that the Compound Parabolic Concentrator (CPC) [15] is the main alternative – a winner optic in different comparison studies and under assessments including efficiency and flux uniformity. On the other hand, the Compound Elliptical Concentrator (CEC) [22] and a recently proposed Aplanat Optic Concentrator (AOC) [33] emerged as secondaries never compared to the CPC. Moreover, CPC optimum geometries reported in a couple of studies [28,29] were confronted to theoretical edge-ray designs [18] to better understand if the CPC geometry really needs to be subjected to optimization when used as an LFC secondary optic.

The results presented in Section 4.1 compares different non-imaging secondary optic designs. Regarding the difference between optimized CPC geometries and edge-ray designs, the developed results indicate that when optical efficiency is the sole objective to be maximized, as in Cheng et al. [28], these two design approaches strongly diverge: the inclusion of the CPC geometry in the set of decision variables to be optimized yields a concentrator with higher efficiency than the edge-ray design, but flux uniformity and acceptance are far lower.

In the case of a two-objective optimization based on optical efficiency and flux uniformity, as in the study conducted by Men et al. [29], results in Section 4.1 show that these two design approaches approximate more than in the case of the efficiency as the sole objective. First, an analysis of the optimum geometries reported by Men et al. [29] shows that all of them refer to non-truncated (full open) CPC optics – as it is done in the theoretical edge-ray design. Then, the practical case with the higher deviation in terms of CPC acceptance angle shows that even in this case the two design approaches yield similar secondary optics, and even more alike when designed with the same gap size. Indeed, the gap size emerges as an important decision variable to play with the trade-off between the optical efficiency, flux uniformity, and acceptance.

The approach of defining CPC geometric parameters as decision variables to be optimized by the search heuristic adds more decision variables to the optimization problem. On the contrary, the edge-rays design does not further complicate the optimization and even presents a clear advantage in the acceptance results.

The results in Section 4.1 show that maximizing efficiency and flux uniformity yields a geometry close to an edge-ray design. Thus, a reasonable hypothesis is that the inclusion of an acceptance objective in the optimization routine would lead to edge-ray solutions for the CPC secondary optic – a subject for future research.

In Section 4.2, a comparison of the AOC and (CPC and CEC) edge-ray designs was presented. The results indicate that the AOC performs poorly in terms of acceptance, however, it presents higher flux uniformity than CPC and CEC and higher efficiency than the CPC. The aplanat decision variables presented by Souza et al. [33] were optimized for a specific value of tube radius, so that a new value (e.g., the 0.035 mm of standard evacuated tubes) would lead to a new search in the aplanat design space. On the contrary, the edge-ray designs are analytical solutions, functions of the tube radius, and no further search is needed, simplifying the design problem.

Finally, the comparison results between CPC and CEC edge-ray designs shows that both optics relate to a trade-off between optical effi-

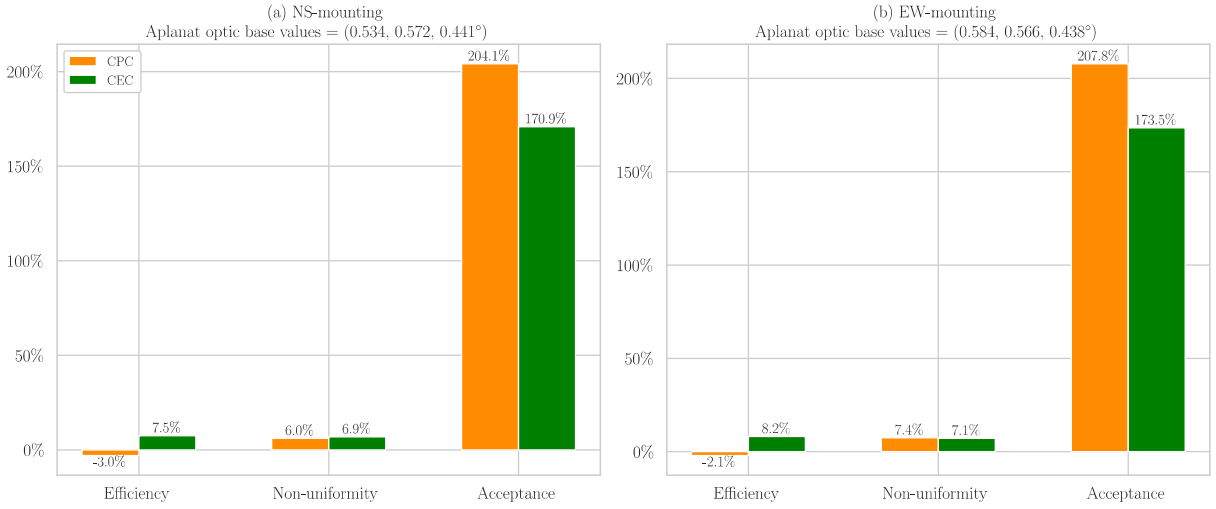

Fig. 17. Relative differences in annual average values of optical efficiency, non-uniformity index, and acceptance half-angle for the optics shown in Fig. 15. It averages results from Fig. 16, considering the TMY data from Evora (N38.53°, W8.0°), and shows the relative differences between CPC and CEC secondaries to the Aplanat optic (see Fig. 15). The Aplanat optic annual average metrics of {efficiency, non-uniformity, and acceptance} are $\{0.534, 0.572, 0.441°\}$ and $\{0.584, 0.566, 0.438°\}$ for NS and EW-mountings, respectively, and are considered as the base values.

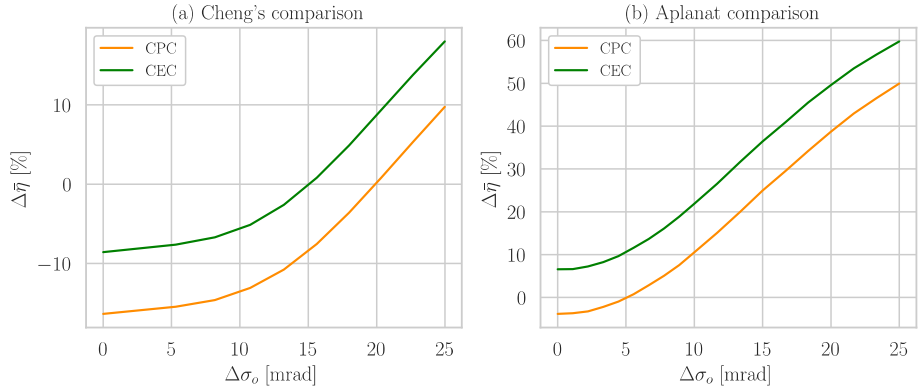

Fig. 18. Relative difference of annual averaged efficiency, $\Delta\bar{\eta}$, as function of additional optical errors, $\Delta\sigma_o$. It shows the relative differences of CPC and CEC edge-rays to (a) Cheng's optic and (b) Aplanat optics. In Figure (a), for the CPC curve (in orange), $\Delta\bar{\eta} = (\bar{\eta}_{\text{CPC}} - \bar{\eta}_{\text{Cheng}})/\bar{\eta}_{\text{Cheng}}$; in Figure (b), for the CEC, $\Delta\bar{\eta} = (\bar{\eta}_{\text{CEC}} - \bar{\eta}_{\text{aplanat}})/\bar{\eta}_{\text{aplanat}}$. This figure shows results for only an NS orientation, as the EW results are quite similar and are not presented here due to conciseness. The results presented in this figure are based on ray-tracing simulations carried out considering the optical settings defined in Table 3 and Table 6. (For interpretation of the references to colour in this figure legend, the reader is referred to the web version of this article.)

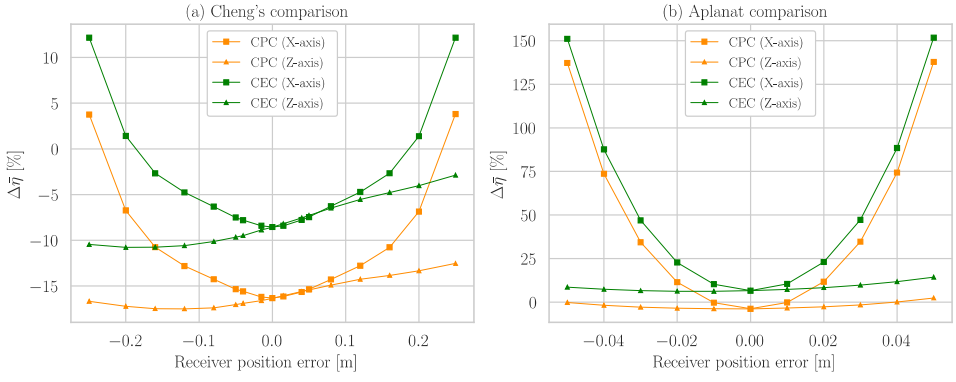

Fig. 19. Relative difference of annual averaged efficiency, $\Delta\bar{\eta}$, as function of receiver position error in both x and z axes. It shows the relative differences of CPC and CEC edge-rays to (a) Cheng's optic and (b) Aplanat optics. In Figure (a), for the CPC curve (in orange), $\Delta\bar{\eta} = (\bar{\eta}_{\text{CPC}} - \bar{\eta}_{\text{Cheng}})/\bar{\eta}_{\text{Cheng}}$; in Figure (b), for the CEC, $\Delta\bar{\eta} = (\bar{\eta}_{\text{CEC}} - \bar{\eta}_{\text{aplanat}})/\bar{\eta}_{\text{aplanat}}$. This figure shows results for only an NS orientation, as the EW results are quite similar and are not presented here due to conciseness. The results presented in this figure are based on ray-tracing simulations carried out considering the optical settings defined in Table 3 and Table 6. (For interpretation of the references to colour in this figure legend, the reader is referred to the web version of this article.)

ciency and acceptance, as represented by $\overline{\eta}$ and $\overline{\beta}$, respectively – the CPC presents the higher $\overline{\beta}$, whilst the CEC has higher $\overline{\eta}$. In terms of flux uniformity, as represented by $\overline{\delta}_q$, the optics do not significantly deviate. Furthermore, as the geometric concentration factor increases, the contour of CPC and CEC optics practically overlaps and, consequently, yield even closer performances.

Concerning to open subjects to be addressed in future works, one is the search for the optimum aplanat decision variables for commercial standard evacuated tubes for high-temperature applications (e.g., the one with a tube radius of 0.035 m). Another topic is an assessment of the similarities between CPC/CEC and Zhu's adaptative design – it has been reported that both optics have a similar shape, although the underlying reasons and the conditions for it have not been fully exploited.

CRediT authorship contribution statement

André Santos: Conceptualization, Investigation, Methodology, Software, Writing – original draft preparation, Visualization, Writing – review & editing. **Diogo Canavarro:** Writing – review & editing, Writing – original draft, Visualization, Validation, Supervision, Methodology, Conceptualization. **Camilo A. Arancibia-Bulnes:** Writing – review & editing, Writing – original draft, Supervision, Methodology, Conceptualization. **Pedro Horta:** Writing – review & editing, Writing – original draft, Visualization, Validation, Supervision, Methodology. **Manuel Collares-Pereira:** Writing – review & editing, Writing – original draft, Visualization, Validation, Supervision, Methodology.

Declaration of Competing Interest

The authors declare that they have no known competing financial interests or personal relationships that could have appeared to influence the work reported in this paper.

Acknowledgments

André Santos acknowledge the financial support by the Fundação para a Ciência e a Tecnologia through the Ph.D. scholarship 2021.07140.BD[1]. Camilo Arancibia-Bulnes thanks the hospitality of the University of Evora's Renewable Energies Chair during the writing of this paper.

References

[1] W.J. Platzer, D. Mills, W. Gardner, Linear Fresnel Collector (LFC) solar thermal technology, in: Concentrating Solar Power Technology, Elsevier, 2021: pp. 165–217. doi:10.1016/B978-0-12-819970-1.00006-2.
[2] M. Collares-Pereira, D. Canavarro, J. Chaves, Improved design for linear Fresnel reflector systems, in: M.J. Blanco, L.R. Santigosa (Eds.), Advances in Concentrating Solar Thermal Research and Technology, Elsevier, 2017: pp. 45–55. doi:10.1016/B978-0-08-100516-3.00003-4.
[3] A. Rabl, Active Solar Collectors and Their Applications, Oxford University Press, New York, 1985.
[4] G. Zhu, T. Wendelin, M.J. Wagner, C. Kutscher, History, current state, and future of linear Fresnel concentrating solar collectors, Sol. Energy 103 (2014) 639–652, https://doi.org/10.1016/j.solener.2013.05.021.
[5] D. Feuermann, J.M. Gordon, Analysis of a two-stage linear fresnel reflector solar concentrator, J. Sol. Energy Eng. 113 (1991) 272–279, https://doi.org/10.1115/1.2929973.
[6] P. Horta, T. Osório, Optical characterization parameters for line-focusing solar concentrators: measurement procedures and extended simulation results, Energy Procedia 49 (2014) 98–108, https://doi.org/10.1016/j.egypro.2014.03.011.
[7] G.S.C. Prasad, K.S. Reddy, T. Sundararajan, Optimization of solar linear Fresnel reflector system with secondary concentrator for uniform flux distribution over absorber tube, Sol. Energy 150 (2017) 1–12, https://doi.org/10.1016/j.solener.2017.04.026.
[8] S. Teske, J. Leung, L. Crespo, M. Bial, E. Dufour, C. Richter, Solar Thermal Electricity - Global Outlook 2016, European Solar Thermal Electricity Association (ESTELA), Brussels, 2016.
[9] M. Collares-Pereira, D. Canavarro, L.L. Guerreiro, Linear Fresnel reflector (LFR) plants using superheated steam, molten salts, and other heat transfer fluids, in: M.J. Blanco, L.R. Santigosa (Eds.), Advances in Concentrating Solar Thermal Research and Technology, Elsevier, Cham, 2017: pp. 339–352. doi:10.1016/B978-0-08-100516-3.00015-0.
[10] RioGlass, RECEIVER TUBES FOR LINEAR CSP (CONCENTRATED SOLAR POWER) APPLICATIONS, (n.d.). https://www.rioglass.com/en/our-products/hce-tubes (accessed August 23, 2023).
[11] F. Burkholder, C. Kutscher, Heat Loss Testing of Schott's 2008 PTR70 Parabolic Trough Receiver, Golden, CO (United States), 2009. doi:10.2172/1369635.
[12] M. Cagnoli, D. Mazzei, M. Procopio, V. Russo, L. Savoldi, R. Zanino, Analysis of the performance of linear Fresnel collectors: Encapsulated vs. evacuated tubes, Solar Energy. 164 (2018) 119–138. doi:10.1016/j.solener.2018.02.037.
[13] W.T. Welford, R. Winston, High Collection Nonimaging Optics, Academic Press, London, 1989 http://linkinghub.elsevier.com/retrieve/pii/0165163390900589.
[14] R. Winston, J.C. Miñano, P. Benítez, W.T. Welford, J.C. Minano, P. Benitez, Nonimaging Optics, Elsevier, Cambridge (2005), https://doi.org/10.1016/B978-0-12-759751-5.X5000-3.
[15] R. Oommen, S. Jayaraman, Development and performance analysis of compound parabolic solar concentrators with reduced gap losses – oversized reflector, Energ. Conver. Manage. 42 (2001) 1379–1399, https://doi.org/10.1016/S0196-8904(00)00113-8.
[16] R. Winston, H. Hinterberger, Principles of cylindrical concentrators for solar energy, Sol. Energy 17 (1975) 255–258, https://doi.org/10.1016/0038-092X(75)90007-9.
[17] R. Winston, Ideal flux concentrators with reflector gaps, Appl. Opt. 17 (1978) 1668–1669, https://doi.org/10.1364/AO.17.001668.
[18] J. Chaves, Introduction to Nonimaging Optics, 2nd ed., CRC Press, New York, 2017. doi:10.1201/b18785.
[19] R. Grena, P. Tarquini, Solar linear Fresnel collector using molten nitrates as heat transfer fluid, Energy 36 (2011) 1048–1056, https://doi.org/10.1016/j.energy.2010.12.003.
[20] D. Canavarro, J. Chaves, M. Collares-Pereira, Simultaneous multiple surface method for linear fresnel concentrators with tubular receiver, Sol. Energy 110 (2014) 105–116, https://doi.org/10.1016/j.solener.2014.09.002.
[21] S. Balaji, K.S. Reddy, T. Sundararajan, Optical modelling and performance analysis of a solar LFR receiver system with parabolic and involute secondary reflectors, Appl. Energy 179 (2016) 1138–1151, https://doi.org/10.1016/j.apenergy.2016.07.082.
[22] D. Canavarro, J. Chaves, M. Collares-Pereira, New dual asymmetric CEC linear Fresnel concentrator for evacuated tubular receivers, in: AIP Conference Proceedings, 2017: p. 040001. doi:10.1063/1.4984397.
[23] G. Zhu, New adaptive method to optimize the secondary reflector of linear Fresnel collectors, Sol. Energy 144 (2017) 117–126, https://doi.org/10.1016/j.solener.2017.01.005.
[24] M. Hack, G. Zhu, T. Wendelin, Evaluation and comparison of an adaptive method technique for improved performance of linear Fresnel secondary designs, Appl. Energy 208 (2017) 1441–1451, https://doi.org/10.1016/j.apenergy.2017.09.009.
[25] R. Abbas, A. Sebastián, M.J. Montes, M. Valdés, Optical features of linear Fresnel collectors with different secondary reflector technologies, Appl. Energy 232 (2018) 386–397, https://doi.org/10.1016/j.apenergy.2018.09.224.
[26] E. Bellos, C. Tzivanidis, A. Papadopoulos, Secondary concentrator optimization of a linear Fresnel reflector using Bezier polynomial parametrization, Sol. Energy 171 (2018) 716–727, https://doi.org/10.1016/j.solener.2018.07.025.
[27] A. Vouros, E. Mathioulakis, E. Papanicolaou, V. Belessiotis, On the optimal shape of secondary reflectors for linear Fresnel collectors, Renew. Energy 143 (2019) 1454–1464, https://doi.org/10.1016/j.renene.2019.05.044.
[28] Z.D. Cheng, X.R. Zhao, Y.L. He, Y. Qiu, A novel optical optimization model for linear Fresnel reflector concentrators, Renew. Energy 129 (2018) 486–499, https://doi.org/10.1016/j.renene.2018.06.019.
[29] J.-J. Men, X.-R. Zhao, Z.-D. Cheng, Y.-K. Leng, Y.-L. He, Study on the annual optical comprehensive performance of linear Fresnel reflector concentrators with an effective multi-objective optimization model, Sol. Energy 225 (2021) 591–607, https://doi.org/10.1016/j.solener.2021.07.051.
[30] H. Ajdad, Y. Filali Baba, A. Al Mers, O. Merroun, A. Bouatem, N. Boutammachte, Particle swarm optimization algorithm for optical-geometric optimization of linear fresnel solar concentrators, Renewable Energy. 130 (2019) 992–1001. doi:10.1016/j.renene.2018.07.001.
[31] A. Ahmadpour, A. Dejamkhooy, H. Shayeghi, Optimization and modelling of linear Fresnel reflector solar concentrator using various methods based on Monte Carlo Ray-Trace, Sol. Energy 245 (2022) 67–79, https://doi.org/10.1016/j.solener.2022.09.006.
[32] H. Beltagy, A secondary reflector geometry optimization of a Fresnel type solar concentrator, Energ. Conver. Manage. 284 (2023) 116974, https://doi.org/10.1016/j.enconman.2023.116974.
[33] L.F.L. de Souza, N. Fraidenraich, C. Tiba, J.M. Gordon, Linear aplanatic Fresnel reflector for practical high-performance solar concentration, Sol. Energy 222 (2021) 259–268, https://doi.org/10.1016/j.solener.2021.05.002.
[34] E.T.A. Gomes, N. Fraidenraich, O.C. Vilela, C.A.A. Oliveira, J.M. Gordon, Aplanats and analytic modeling of their optical properties for linear solar concentrators with tubular receivers, Sol. Energy 191 (2019) 697–706, https://doi.org/10.1016/j.solener.2019.08.037.
[35] Y. Qiu, M.J. Li, K. Wang, Z. Bin Liu, X.D. Xue, Aiming strategy optimization for uniform flux distribution in the receiver of a linear Fresnel solar reflector using a multi-objective genetic algorithm, Applied Energy. 205 (2017) 1394–1407. doi:10.1016/j.apenergy.2017.09.092.

[1] https://doi.org/10.54499/2021.07140.BD.

[36] A.V. Santos, D. Canavarro, P. Horta, M. Collares-Pereira, On the comparison of parabolical and cylindrical primary mirrors for linear Fresnel solar concentrators, Renew. Energy 218 (2023) 119380, https://doi.org/10.1016/j.renene.2023.119380.
[37] J. Ma, C.-L. Wang, Y. Zhou, R.-D. Wang, Optimized design of a linear Fresnel collector with a compound parabolic secondary reflector, Renew. Energy 171 (2021) 141–148, https://doi.org/10.1016/j.renene.2021.02.100.
[38] Y. Qiu, Y.L. He, Z.D. Cheng, K. Wang, Study on optical and thermal performance of a linear Fresnel solar reflector using molten salt as HTF with MCRT and FVM methods, Appl. Energy 146 (2015) 162–173, https://doi.org/10.1016/j.apenergy.2015.01.135.
[39] R. Abbas, J.M. Martínez-Val, Analytic optical design of linear Fresnel collectors with variable widths and shifts of mirrors, Renew. Energy 75 (2015) 81–92, https://doi.org/10.1016/j.renene.2014.09.029.
[40] T. Wendelin, A. Dobos, A. Lewandowski, SolTrace: a ray-tracing code for complex solar optical systems, golden, CO (united States) (2013), https://doi.org/10.2172/1260924.
[41] A.V. Santos, soltracepy: a Python module for the fast implementation of SolTrace ray-tracing simulations, (2023). doi:10.5281/zenodo.10439687.
[42] W.F. Holmgren, C.W. Hansen, M.A. Mikofski, pvlib python: a python package for modeling solar energy systems, Journal of Open Source Software. 3 (2018) 884, https://doi.org/10.21105/joss.00884.
[43] I. Reda, A. Andreas, Solar position algorithm for solar radiation applications, Sol. Energy 76 (2004) 577–589, https://doi.org/10.1016/j.solener.2003.12.003.